Chapter 2

In Situ Transmission Electron Microscopy for Electronics

Masashi Arita, Kouichi Hamada, Yasuo Takahashi,
Kazuhisa Sueoka and Tamaki Shibayama

Additional information is available at the end of the chapter

http://dx.doi.org/10.5772/60651

Abstract

Electronic devices are strongly influenced by their microstructures. *In situ* transmission electron microscopy (*in situ* TEM) with capability to measure electrical properties is an effective method to dynamically correlate electric properties with microstructures. We have developed tools and *in situ* TEM experimental procedures for measuring electronic devices, including TEM sample holders and sample preparation methods. The method was used to study metallic nanowire by electromigration, magnetoresistance of a ferromagnetic device, conductance quantization of a metallic nanowire, single electron tunnelling, and operation details of resistive random access memories (ReRAM).

Keywords: *In situ* TEM, TEM sample holder, electromigration, magnetoresistance, tunnel conduction, resistive RAM

1. Introduction

Transmission electron microscopy (TEM) has been efficiently used in a variety of research fields. It is possible to observe individual atoms by using up-to-date microscopes. In addition to conventional (static) TEM observation and microanalyses, dynamical observations and recording is possible under controlled conditions. While *in situ* TEM has already been utilized in early years [1, 2, 3], this method has attracted much attention in recent years because the atomic or nanoscale observations can be performed with simultaneous physical/chemical measurements. This type of investigation can be done without changing the TEM construction by using specially designed TEM holders such as TEM holder with a piezo actuator (even

without the feedback system, it will be called the TEM/STM (scanning tunneling microscopy) holder in this report) [4, 5, 6, 7, 8].

In the research field of electronics, next-generation electronic devices are now under development from the perspective of power consumption, high integration as well as high functionality. The electronic properties of these devices have strong relationship with their crystallographic and/or magnetic microstructures which occasionally change during the device operation. Therefore, the importance of the *in situ* TEM is increasing to understand the operation mechanism in detail. Since the year of 2000, we have developed various types of TEM holders for *in situ* TEM of electronic devices. In this article, we will explain developed *in situ* TEM holders and present effectiveness of this method to magnetic RAM (MRAM) [9, 10], single-electron devices (SED) [11, 12], resistive RAM (ReRAM) [13, 14, 15], as well as electromigration [16, 17, 18, 19].

2. *In Situ* TEM system for electric measurements

There is a schematic of the *in situ* TEM system in Fig. 1(a), which is composed of a custom-made TEM holder, a holder control system if needed, an electric measurement system, and a charge-coupled device (CCD) camera system (30 ms/frame). All the image data including those from the personal computer (PC) display are superposed on one another when needed. The TEM instruments were JEM 2010 (200 kV, C_s = 0.5 mm) and JEM 200CX (200 kV) microscopes, whose vacuum was 10^{-4}–10^{-5} Pa. Figures 1(b) and 1(c) have control diagrams of the electromagnet holder and TEM/STM holder developed in this work. These systems have plural voltage/current sources controlled by a PC. Various types of electric measurements were carried out depending on the purpose. Conventional instruments such as an electric source, a digital multimeter, a source-measure-unit (SMU), and a digital oscilloscope were used. The system in Fig. 1(d) is for conventional 4-terminal measurements, that in Fig. 1(e) is for TEM/STM experiments with high-speed measurements, and that in Fig. 1(f) is for multipurpose usage using TEM/STM.

3. TEM holders developed for *in situ* electronic experiments

Three types of TEM holders were developed in this work. They were holders for current measurements of patterned media, a holder with electromagnets used for Lorentz TEM (LTEM), and TEM/STM holders. Their details are described in the following subsections.

3.1. Holders having four or multiple terminals to investigate patterned devices

There is a photograph of two custom-made single-tilt TEM holders with four electric terminals in Fig. 2(a). The samples are placed at position 1. Figures 2(b) and 2(c) are enlarged photographs. Samples of less than about 5 × 5 mm can be investigated. The sample electrodes were connected to two current terminals (I) and two voltage terminals (V). These terminals are

http://dx.doi.org/10.5772/60651

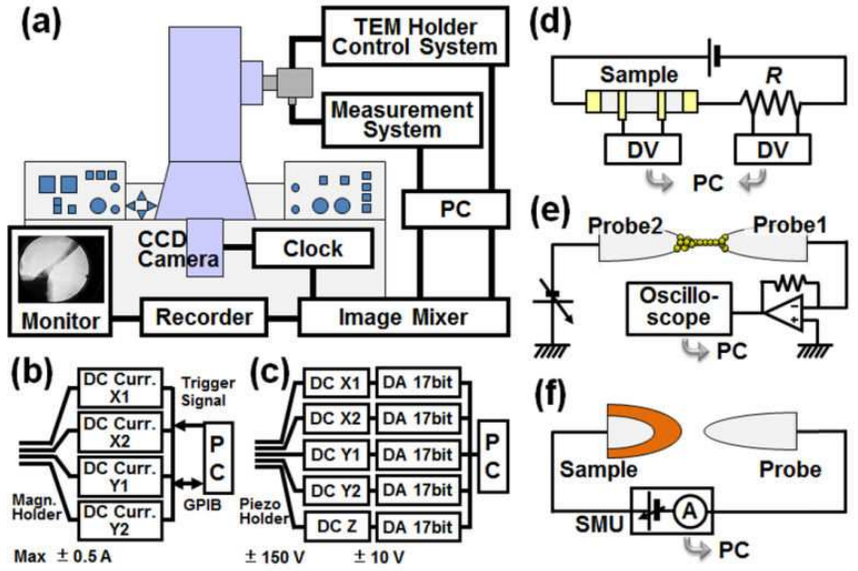

Figure 1. (a) Schematic of system. Diagrams of (b) electromagnet and (c) TEM/STM holders. Measurement systems for (d) four terminal method, (e) high-speed measurements, and (f) TEM/STM.

connected to four co-axial connectors (denoted as 2 in Fig. 2(a)). The shield lines of the cables are floated from the TEM holders, which are connected to the ground level (JEM200CX) or a certain voltage level (~2 V for JEM2010). Therefore, they can be used as the guard lines for low current measurements. These holders were mainly used for LTEM observations in this work. There are photographs of a double-tilt holder with 16 terminals in Figs. 2(d) and 2(e) [19]. The sample (turned upside down) was placed at the centre of the holder to face the terminals (Fig. 2(d)). When the cover is closed, the sample electrodes connect automatically with the terminals for electrical measurements (Fig. 2(e)). Multiple devices can be measured during one experiment by using this holder, which was used mainly to investigate electromigration.

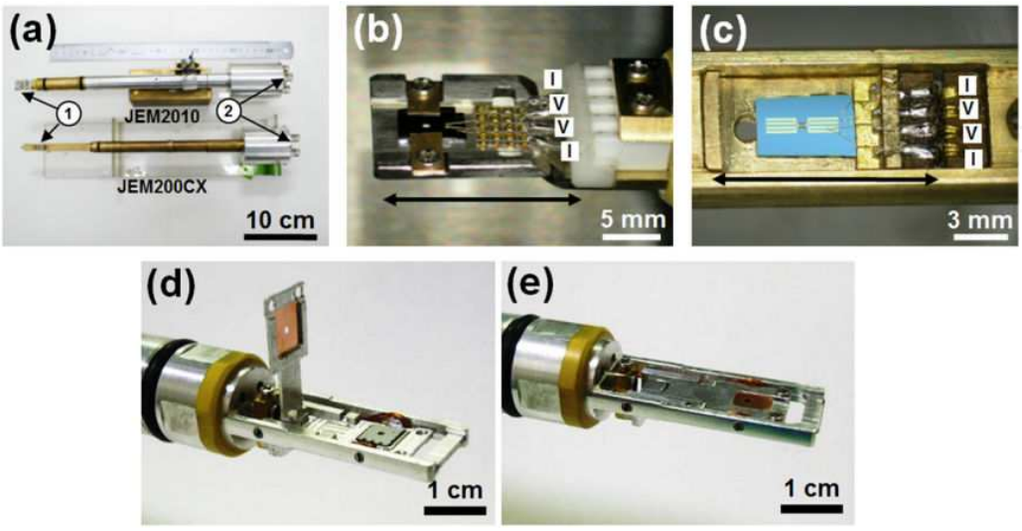

Figure 2. (a) TEM holders for four-terminal electrical measurements. Enlarged image of TEM holder head for (b) JEM2010 and (c) JEM200CX. (d) and (e) Double-tilt TEM holder having 16 electrodes.

3.2. Holder generating in-plane magnetic field

Magnetic devices are important in electronics. *In situ* observations of magnetic microstructures by LTEM should provide key information. The in-plane field of film devices can be varied by tilting the sample [20, 21, 22, 23] in the remanence field of the TEM objective lens (LowMag-mode). While this is quite simple, the field is single-axial, and the speed is slow. The installation of electromagnets effectively overcomes these problems, and speedy field control can be achieved. The TEM holder has coils on board in some cases [24, 25], which is an advantage for conventional TEM users. However, when coils generate a magnetizing field, the TEM electron beam is deflected, and the image is fatally shifted. Therefore, beam-deflection-back coils [2, 24, 25, 26, 27] should be installed. A TEM specimen holder with an electromagnet system needs to be developed, which generates a double-axial magnetic field and compensates beam deflection. This section presents a TEM holder with two miniaturized four-pole electromagnets [28]. *In situ* electrical measurements were made possible by using this holder with four terminals.

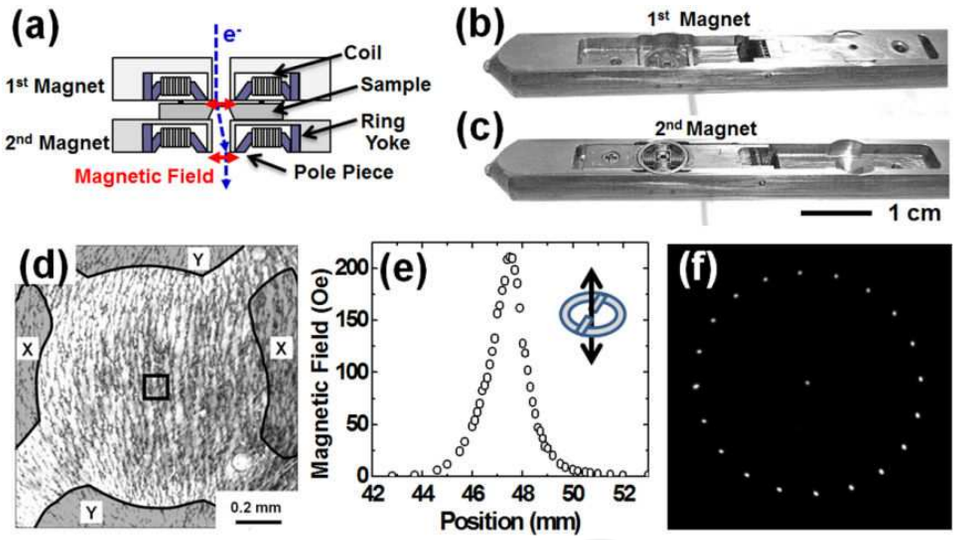

Figure 3. Electromagnet holder. (a) Cross-section of magnet system. Holder head (b) before and (c) after sample was placed. (d) Distribution of magnetic field. X and Y are pole pieces of electromagnet. Square at the centre is a region for observation. (e) Magnetic field in pole gap along arrow in schematic of magnet (inset). (f) Example of deflection of electron beam by electromagnet.

Figure 3(a) is a schematic cross section of the double-layer magnet system where a sample is sandwiched between two four-pole electromagnets. Each electromagnet is assembled from two perpendicularly oriented two-pole electromagnets with ring-shaped yokes (ϕ7 mm and gap of 1 mm). Two serially connected coils with ~30 turns are wound onto each two-pole magnet (maximum current: 500 mA). In-plane magnetic field can be applied to the sample along any direction. The first magnet was used to generate the magnetic field applied to the sample. Electron beam used for TEM observations were deflected by this field. The second magnet below the sample is used to compensate for this deflection. This prevented the TEM image from experiencing fatal deformation or movement. In addition, four electric terminals

http://dx.doi.org/10.5772/60651

were arranged in the chinks of the first magnet. Figures 3(b) and 3(c) are photographs of the TEM holder. This is a side entry holder designed for JEM-200CX. The sample is placed by facing it against the magnet. When it was fixed by closing the cover, the contact pads of the sample automatically made contact with the electrodes.

The maximum magnetic field between the pole pieces was measured to be 214 Oe at 500 mA by using a Hall probe. A software package was developed to compensate the hysteretic features of the magnet, and the generated field could be controlled with an accuracy of 1 Oe or better. The homogeneity of the field was checked by using Fe powder suspended in oil, as seen in Fig. 3(d), where only magnet Y was excited. The field within the LTEM observation window was homogeneous (square at the centre: 100 x 100 μm). The distribution of the magnetic field is shown in Fig. 3(e). The current through the coils was 500 mA. The magnetic field was ~7 Oe at 2.5 mm from the pole piece. Thus, there is almost no influence from the second magnet on the specimen: They were 2.5 mm apart from each other. One of the four-pole electromagnets was activated to generate a rotating field (38 Oe). The beam deflection with various magnetic fields was recorded in multi-exposed images (Fig. 3(e)). The beam spot was circularly moved. Excellent controllability of the field was achieved.

The LTEM image moved fatally due to beam deflection caused by the first electromagnet. There is an example in Fig. 4(a) where images with H_x = +9 Oe (along the right) and –9 Oe (along the left) are superposed on a wide-range image under 0 Oe. The image moved by about ±33 μm. The second electromagnet was simultaneously activated to compensate this image movement. The resulting images are compared in Fig. 4(b) where image movement decreased significantly.

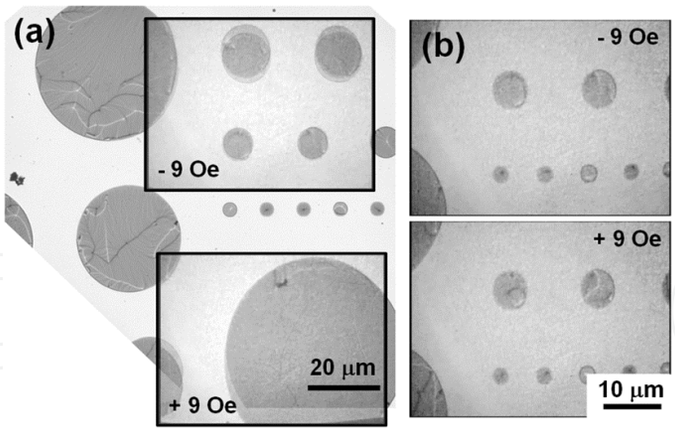

Figure 4. (a) Shift in CCD image (±9 Oe along right). Two CCD images are superposed on wide-range image. (b) CCD images taken with beam-deflection-back-system. Image movement was compensated for. LTEM images were taken using the Fresnel method in LowMag-mode.

3.3. TEM/STM holder

There is a schematic of a specimen holder fitted to a JEM 200CX microscope in Fig. 5(a) and photographs of this in Fig. 5(b) [8]. The probe was coarsely moved with three mechanical

micrometres (stroke: 0.2 × 0.2 × 10 mm). A piezo tube was placed at the left end of the column pole, with which the position of the probe was controlled at a rate of 400 nm/V (perpendicular to the column pole) and 30 nm/V (along the column pole). The maximum voltage was 100 or 150 V. Two probes could be attached to the piezo actuator. One of two electrodes placed at the piezo actuator could be selected without breaking the vacuum by rotating the column pole using a stepping motor. Figure 5(c) is a photograph of a holder designed for the JEM 2010 microscope [29]. Three electrodes could be placed in this TEM holder (two probes and one sample). The sample was directly connected to the voltage source using a coaxial cable, where the probes were connected to an in-column amplifier for nA measurements or an ammeter. While the basic design of the holders developed here may be the same as that of commercially available holders, additional functions such as multiple probing can be added through custom designing. It is quite important to design the piezo actuators and mechanism for coarse movement to enable the holder to be easily handled.

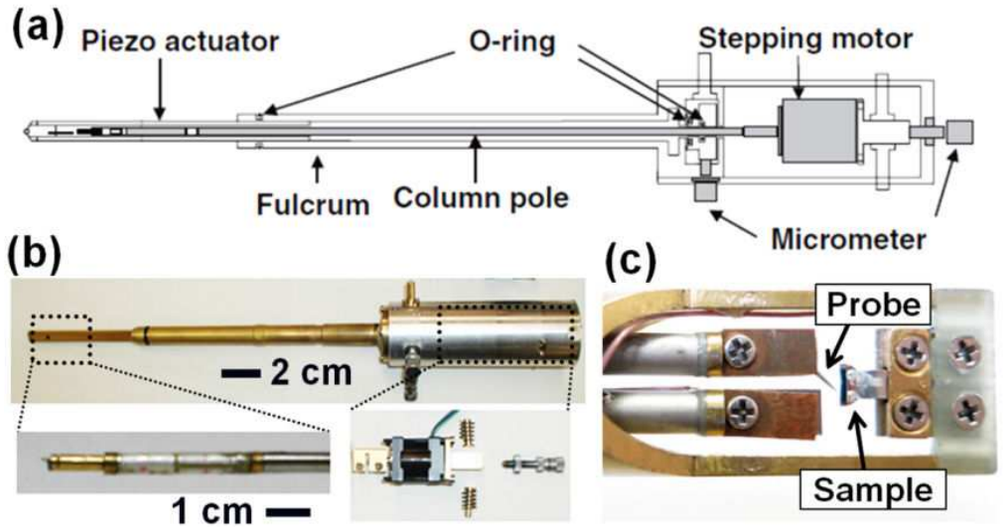

Figure 5. (a) Schematic and (b) photograph of TEM/STM holder for JEM200CX. Electrode and sample were placed inside. (c) Holder for JEM2010. Needle probe was moved to contact to fixed sample.

4. Sample preparation method

Our main purpose here is to develop *in situ* TEM that can be applied to electronic devices whose electrical properties have correlations with geometric and/or magnetic microstructures. Special sample preparation techniques were required to achieve this. One of them is the use of an Si_3N_4 membrane on which electronic devices are patterned. A method of fabricating TEM observation windows without inducing any electric leakage will be briefly described. Another method was used in the TEM/STM observations. The focused ion beam (FIB) method is widely utilized to observe electronic films and devices. However, it was time consuming and not cost effective because the samples are frequently destroyed during *in situ* experiments, for example,

http://dx.doi.org/10.5772/60651

ReRAM samples. This section describes also a method of preparing needle-shaped or wedge-shaped metallic (or Si) substrates for thin film deposition.

4.1. Patterned devices on SiN/Si substrate with observation window

Since the invention by Jacobs and Vehoeven [30], many electron microscopists focused their attention on the use of free-standing Si_3N_4 membranes as substrates [31]. These membranes are extremely flat and insulating and are now commercially available. However, it is important to prepare substrates and patterned devices on demand because we can design a variety of patterns by ourselves to carry *in situ* TEM observations on patterned electronic devices. The starting material was a Si_3N_4/Si wafer. The Si_3N_4 layer (25 or 35 nm thick) was formed on a 525-μm thick Si (001) wafer by chemical vapour deposition (CVD). The wafer was cut into pieces of 20 × 20 mm, and the sample preparation was done by combining the four processes (A-D) in the following text. There are some examples of the TEM samples in Fig. 6. While the samples in Figs. 6(a) and 6(b) [32] are for electric measurements, the one in Fig. 6(c) is only for TEM observation without electrodes.

(A) **Patterning of Si_3N_4 on backside of Si wafer**: This process involves the fabrication of the mask to chemically etch the Si wafer to form observation windows. We used photolithography followed by reactive ion etching (RIE, CF_4: O_2 = 4: 1) when high levels of accuracy were required. This process could be replaced by scratching with a diamond pencil if only rough positioning was required.

(B) **Patterning of devices**: Electrodes of $Au_{(30\ nm)}/Ti_{(10\ nm)}$ were formed on the front surface by using double layer photolithography of OFPR800/PMGI followed by lift-off. After this, the sample patterns such as Au or permalloy ($Ni_{81}Fe_{19}$, abbreviated as Py) were prepared by using the electron-beam lithography of ZEP/PMGI and lift-off or photolithography. Deposition by using a metal mask was used when rough positioning was required.

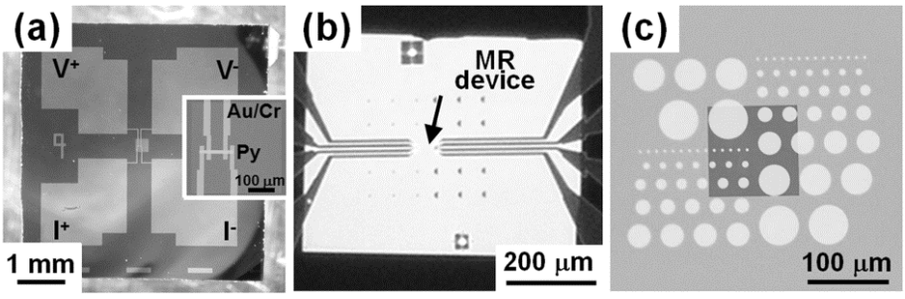

Figure 6. Py patterns prepared on Si_3N_4/Si substrates, (a) pattern for AMR measurements, (b) MR cantilever, and (c) disks to observe magnetic vortices. Square at centre in (a) or (c) is an observation window. Pads marked with V are voltage terminals, and those marked with I are current terminals.

(C) **Chemical etching to form windows**: To obtain a free-standing Si_3N_4 membrane, potassium hydroxide (KOH) etching at 80°C was done from the backside of the Si wafer. When patterning was carried out after this etching process, the substrate was simply dipped in the KOH aqueous solution. When the patterning was done before etching, a specially designed etching holder

made of Teflon was used to protect the pattern from the chemical. The window size was typically between 100 × 100 and 500 × 500 μm.

(D) **Cutting of the sample into small pieces**: TEM holders (Figs. 2 and 3) were developed for the sample size of 5 × 5 mm. Substrates with or without devices were cut into this size by cleaving the Si wafer.

4.2. Needle-shaped and wedge-shaped probes and substrates

The probes used in the TEM/STM experiments were prepared with methods based on ion milling. This is because very sharp probe apexes were required to select local areas to be measured. In addition, when the probe was used as the substrate for sample film deposition, its apex should be thin enough for high resolution TEM (HRTEM).

The ion-shadow method [33] was used for probe fabrication, which is a sputtering technique using powders (mask material) with low sputtering rate. After the probe material was mechanically sharpened into a cone, the mask particle (e.g., diamond or carbon: ϕ10 μm) was put on the top, and the Ar^+ ion sputtering was performed. During sputtering, the unmasked part of the tip material is etched, and the particle size was reduced. Finally, a fine cone was obtained when the powder was completely sputtered out within ~1 hour (Fig. 7(a)). While the underlying principles of this process are the same as that of ion-beam lithography, the use of the powder masks is essential in the ion-shadow method. There are examples in Figs. 7(b) and 7(c). The radius of curvature of the apex was usually ~20 nm or less.

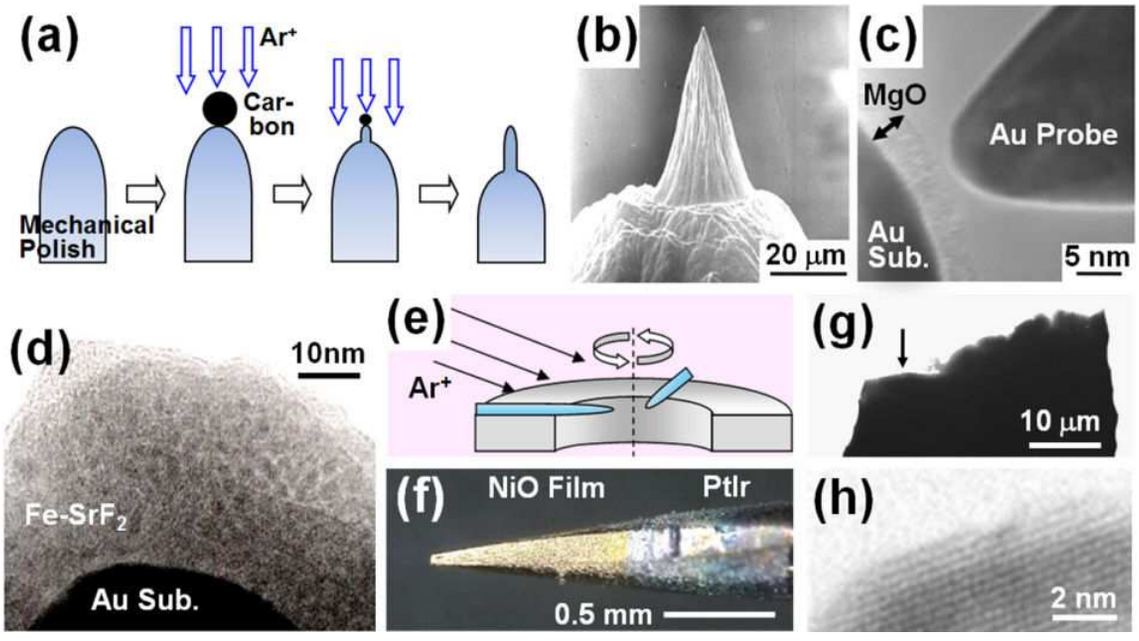

Figure 7. (a) Ion-shadow process forming cone-shaped probe. (b) Scanning electron microscopy (SEM) image of Au probe. (c) TEM image of Au probe approaching the MgO layer on Au substrate. (d) Fe-SrF_2 film on needle-shaped Au substrate. (e) Schematic of thinning process of substrate. (f) Optical micrograph of wedge-shaped PtIr substrate covered by NiO film. (g) TEM image of wedge-shaped PtIr substrate. Arrowed region is magnified in (g).

The probe can be used as the substrate for film deposition [8]. After the tip-shaped apex had been fabricated, the probe was washed with acetone and ethanol in an ultrasonic bath. It was annealed at 420 K for 30 min, and film deposition was done. One example can be seen in Fig. 7(c), where thin MgO was deposited on the "Au Sub." There is another example in Fig. 7(d), where a composite film of Fe–SrF_2 (~37 vol% Fe, 40 nm thick) was deposited at RT. The round grey contrast denotes Fe particles with sizes of ~2.7 nm.

Another method of fabricating very sharp probe is shown in Fig. 7(e). Commercially available STM tips or mechanically ground probes were sharpened using ion milling from backside with rotation. An apex of 10 nm or less was obtained. When the probe is used as a substrate, it is better to be wide to enable multiple investigations. For this purpose, the probe material was mechanically ground into a wedge and ion milled [34]. There is a micrograph of NiO on PtIr in Fig. 7(f), while TEM images are shown in Figs. 7(g) and 7(h). The substrate was about 50 μm wide and thin enough to observe lattice fringes.

4.3. Easy method to prepare miniaturized multilayer devices for *in situ* TEM

In situ investigation on multilayer devices is important for electronic devices, and FIB is one of the methods of fabricating these TEM samples. However, it is time consuming and costly, while devices can occasionally be easily destroyed. For example, current jump at resistive switching of ReRAMs induces overshoot current, and the samples are quite likely to be destroyed. We focused on the ion-shadow method and applied it to the sample preparation of multilayer films formed on Si wafers. A film on a substrate was cut into small pieces (e.g., 100 μm × 2.5 mm). Carbon spheres (10–30 μm) were used as the mask material. A drop of slurry was dripped onto a glass plate and dried, and the particles were transferred to the substrate by lightly scrubbing the glass surface. Next, a milling process (Ar^+, 5 kV, 1 mA) was carried out for 1 hour by using a milling apparatus for TEM. The ion beam was almost perpendicular to the substrate surface. As a result, a sample with needle-shaped projections would be prepared as shown in Fig. 8(a) [35].

Figure 8(b) has scanning electron micrographs (SEMs) over a wide area. Many needles can be identified on the Si surface. There are magnified images from two different regions in Figs. 8(c) and 8(d). A sharp needle 5 μm in length can be seen at around the beam centre (Fig. 8(d)). No carbon particle residuals can be identified at this magnification, and we can expect a small fragment of the film on the needle. On the other hand, the needle lengths are short, and large carbon residuals are identified in Fig. 8(c), which was away from the centre by 500 μm. The carbon residuals and the sample film on the apex should be completely etched out around the beam centre by increasing the milling time. However, the carbon residuals should become small at the neighbouring regions, and needles with adequate apex size should appear. There must be regions with needles suitable for *in situ* TEM somewhere on the substrate, independently of the milling time. Several needles with ReRAM fragments were obtained in one TEM sample. There is a top-view SEM micrograph in Fig. 8(e), where the needle had a symmetric cone shape. An example of the TEM image is in Fig. 8(f), which is a multilayer film ($Pt_{(100\ nm)}/Cu_{(30\ nm)}/MoO_{x\ (50\ nm)}$ on a TiN/Si substrate). The sample was ϕ230 nm and usable for

in situ TEM. No fatal current leakage appeared when the bias voltage was applied between Pt and Si.

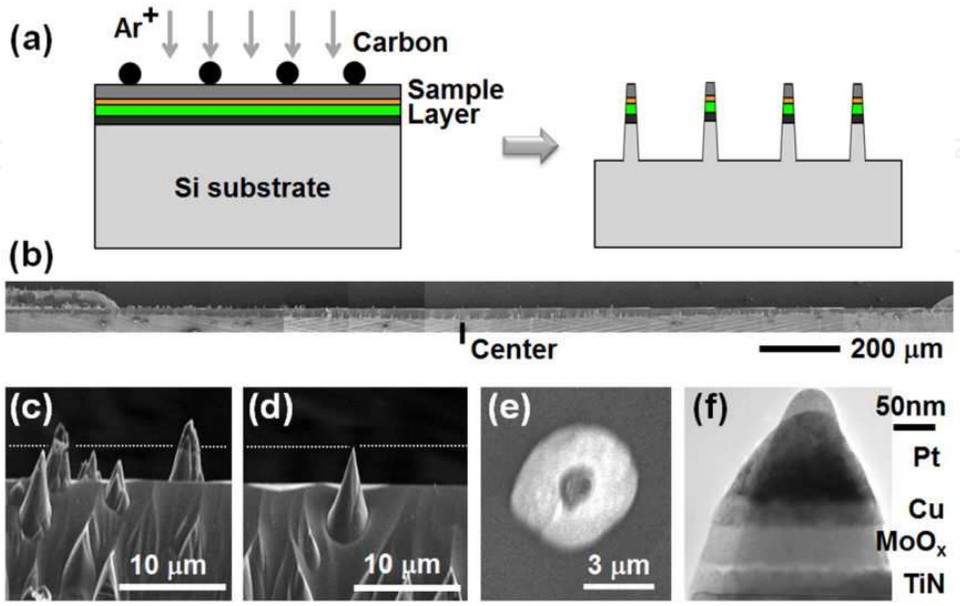

Figure 8. (a) Schematic of ion-shadow process. (b) SEM of needles formed at Si substrate. Magnified images (c) 500 μm left of beam centre and (d) at beam centre. Lines denote Si surface before milling. (e) Top view SEM of needles having regular shape. (f) TEM cross section of multilayer film.

5. Application of developed TEM holders

5.1. Electromigration

Electromigration (EM) is the term used for the electrically induced atom movement after momentum transfer from electrons. It causes failure in the wiring [36], and the researchers on LSI have tried to suppress it. However, EM has attracted a great deal of attention in creating metallic nanogaps used in SEDs as well as switching devices [37, 38]. Researchers in this field have developed methods of enhancing EM. It is important to achieve high levels of control for EM in both cases even though their purposes have differed. *In situ* TEM [17, 18, 39] can provide important information on this phenomenon. In this work, Au wire patterns were investigated with the current density of 10^9 A/cm^2 or more [19]. The operation system is in Figs. 1(a), 1(d) (using an SMU), and 2.

Atom transportation along the electron flow was identified in TEM images extracted from a video (Fig. 9). When a positive voltage was applied to the right of Fig. 9(a), narrowing occurred at the upstream side of the electron flow (left part of Fig. 9(b)). With polarity inversion, the left end of the wire gained area while the right end lost area (Fig. 6(c)). This morphological change during polarity inversion fits well with earlier reports [18]. Narrowing occurred at the upstream side, and widening on the downstream side, which was independent of the voltage

polarity. This suggested that Au atoms were transported along the same direction as that of the electron flow (i.e., opposite to current).

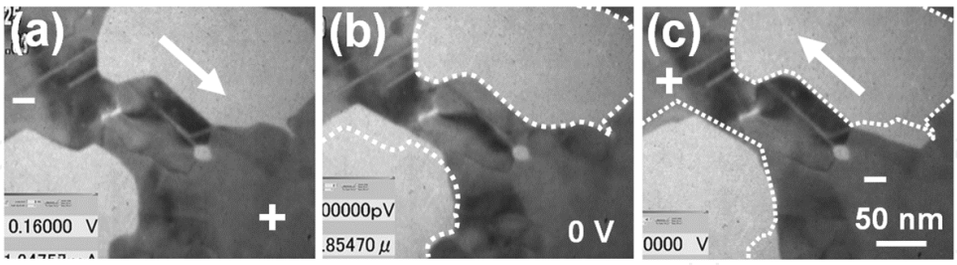

Figure 9. Sequential change in wire geometry during current reversion. Arrows are along electron flow. Broken lines in (b) and (c) correspond to edges in (a) and (b).

The metallic wire narrowed due to EM. The narrowing rate was not monotonous over time. The wire thinning occasionally started at a certain time, then stopped, and restarted. The wire thickened in some cases. There is an example in Fig. 10 where wire narrowing is evident near the surface step. The edge on the downstream side of the step (dotted line) retreated in Fig. 10(b) (5.25 seconds after Fig. 10(a)), while the edge on the upstream side (solid line) only retreated slightly. As a result, the step increased and cleared. The step started to collapse at the corner in Fig. 10(c). This collapse propagated to neighbouring regions in Fig. 10(d). The upstream side lost atoms in Figs. 10(e), and the downstream side gained atoms. Curve C on the upstream side has a sudden drop in wire width as can be seen in Fig. 10(g), while curve B on the downstream side has a gradual increase. Curve A apart from the step exhibits less change. The width at B reached maximum, and a new narrowing process. The wire narrowing accelerated when the step collapsed. Although only two examples have been presented in this report, contributions on wire narrowing and gap formation from various singularities such as grain boundaries and stacking faults can be investigated with the method used in this research.

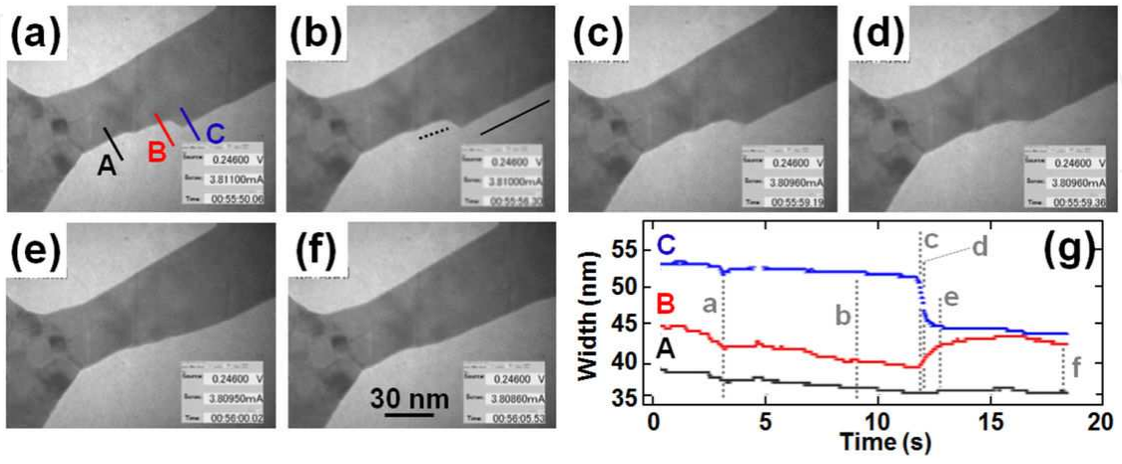

Figure 10. Collapse of surface step and wire narrowing. (a)-(f) Video images and (g) wire width at positions A to C. Electron flew from the right to the left (current: left to right).

5.2. Magnetic domains and magnetoresistance of ferromagnetic devices

Magnetic devices are one of the most important subjects in electronics. Their physical properties, such as magnetoresistance (MR) and magnetization reversal, are influenced by their magnetic microstructures. Therefore, the magnetic microstructures of tiny magnetic patterns have been investigated by using various techniques. *In situ* observations of magnetic microstructures when magnetic fields are applied should provide key information about these mechanisms. The LTEM explained in this section is one method that can clarify these operation mechanisms.

5.2.1. Experiments by using conventional current measurement holder

An $Ni_{79}Fe_{21}$ film (Py, 2 mm × 100 μm, 35 nm thick) was deposited by using a metal mask. Magnetic anisotropy was induced during the deposition by applying 300 Oe along the long axis of the pattern. It was composed of grains with a size of ~10 nm. The system is outlined in Figs. 1(a) and 1(d), and the holders are seen in Figs. 2(a)-(c). The effective magnetic field in the film plane was controlled by specimen tilt [20, 21, 22, 23]. The observations were carried out in the LowMag-mode, in which the TEM objective lens was switched off. While the residual field (43 Oe) of the objective lens was usually used, ~200 Oe was generated with external current through the lens coil if necessary. The in-plane field was $H = H_0 \sin\phi$, whereas H_0 is the field of the TEM lens and ϕ is the tilting angle. Because the film was thin, the influence from the out-of-plane component could be neglected. The magnification of the Lorentz images was usually × 600. The images were taken with the Fresnel method.

There are typical LTEM images in Figs. 11(a)-(c) with the simultaneously measured MR-curve, where magnetic field was applied downward in the image (perpendicular to the current) [40]. This was the transverse anisotropic magnetoresistance (AMR). The voltage electrodes are visible as dark parts on the left and right of the image. The fine image contrast in the shape of curves from the top to the bottom edges, called "ripple," reflects the spatial fluctuations in the magnetic moment in local areas. The averaged magnetic moment, *M*, in any local area is directed perpendicularly to the ripple (arrows). The resistance of the film varied between 35.68 and 35.94 Ω. The MR ratio defined as

$$MR(\%) = 100 \times (R_{max} - R) / R_{max} \quad (1)$$

was 0.7% at 25 Oe, where R_{max} and R were the maximum resistance and the resistance at a certain H. The ripple contrast was almost linear in a low field (Fig. 11(a)). The directions of local M at the top edge (A), the centre (B), and the bottom edge (C) were horizontal because of induced and shape anisotropy. Resistance was maximum. In Fig. 11(b) with 10 Oe, the resistance decreased and ripple contrast was bent (Fig. 11(b)). Local M rotated downward, but rotation angles θ (plus: clockwise) at both edges were smaller than those at the centre. The curvature of the ripple increased with field, and the resistance was further reduced. Strongly bent ripple contrasts were observed in areas 20 μm from the edges (Fig. 11(c)) when the field was beyond the inflection point of the MR-curve. On the other hand, the ripple in the innermost

http://dx.doi.org/10.5772/60651

part was almost linear, indicating almost downward M. The distribution of θ is summarized in Fig. 11(d) for various in-plane fields. The positions of 0, 50, and 100 μm correspond to A, B, and C in Fig. 11(a), respectively. The influence of the edges can clearly be identified.

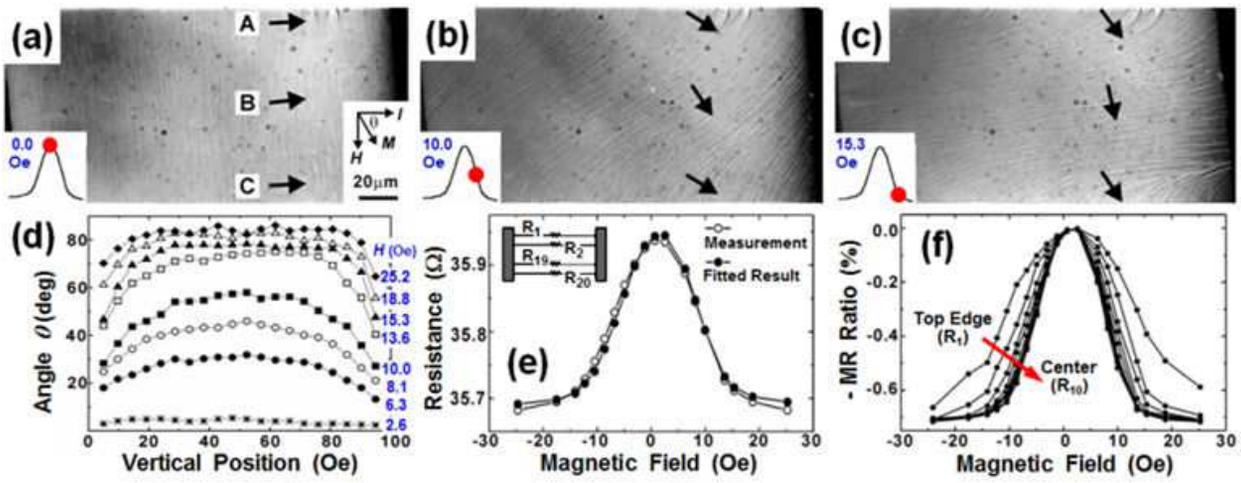

Figure 11. (a)-(c) LTEM images with MR-curves (inset). Relation between orientation of current I, H, and M is in (a). Distortion of images due to specimen tilt is corrected. Arrows are average directions of M at A, B, and C. (d) Angle θ as a function of vertical position from top (0) to bottom (100). (e) Fitted MR-curve using model (inset) compared with measured curve. (f) Estimated MR-curves at local areas between A and B.

Resistance R changes accordingly to

$$R = R_0 + \Delta R \cos^2\theta, \tag{2}$$

whereas R_0 is resistance when the magnetization is perpendicular to current, and ΔR is maximum change in resistance. Resistance and the MR-ratio change from place to place due to the inhomogeneity of M. Considering a model where the film is composed of 20 striped resistors parallel to the edges, the resistance was analysed as

$$1/R = \sum_{i=1}^{20} \left(1/R_i\right),\ R_i = 20\left(R_0 + \Delta R \cos^2\theta_i\right). \tag{3}$$

Here, R_i and θ_i are the resistance and angle θ of the i-th resistor. Least-square fitting was performed as seen in Fig. 11(e). The result from calculation agreed well with the measurements where R_0 = 35.69 Ω and ΔR = 0.26 Ω. The MR-curves at local areas were estimated by using these parameters and the observed θ_i, as shown in Fig. 11(f), where only the upper half of the pattern (R_1 to R_{10}) was evaluated. The MR-curve was broad at the edge (R_1). It became narrow near the central part of the film. We concluded on the basis of the results here that the main influence of the edges on the MR-curve extended ~20 μm.

Next, a Py stripe pattern was deposited at 500°C under a field of 300 Oe along the short axis to induce uniaxial magnetic anisotropy. *In situ* experiments with a field along the easy axis (perpendicular to the long axis) were carried out (Fig. 12). In this case, the AMR effect caused by changes in the ripple structure and appearance/disappearance of magnetic domain walls (DWs) could directly be investigated without any influence from the rotation of the magnetization [41]. H_0 was set to be 248 Oe by using external current to the TEM lens coil. The MR curve measured in the microscope is plotted in Fig. 12(a). The MR-ratio was 0.86% at 200 Oe. Separation in the MR curve was ±45 Oe. *In situ* TEM experiments were performed from +20 to +125 Oe (red curve in Fig. 12(a)). The micrographs in Fig. 12(b) correspond to A to D in Fig. 12(a). When the field is positive, it orients downward in these images. The black contrast on the right and left of the images denotes Au voltage terminals. Thus, all regions contributing to the MR effect in Fig. 12(a) can be seen.

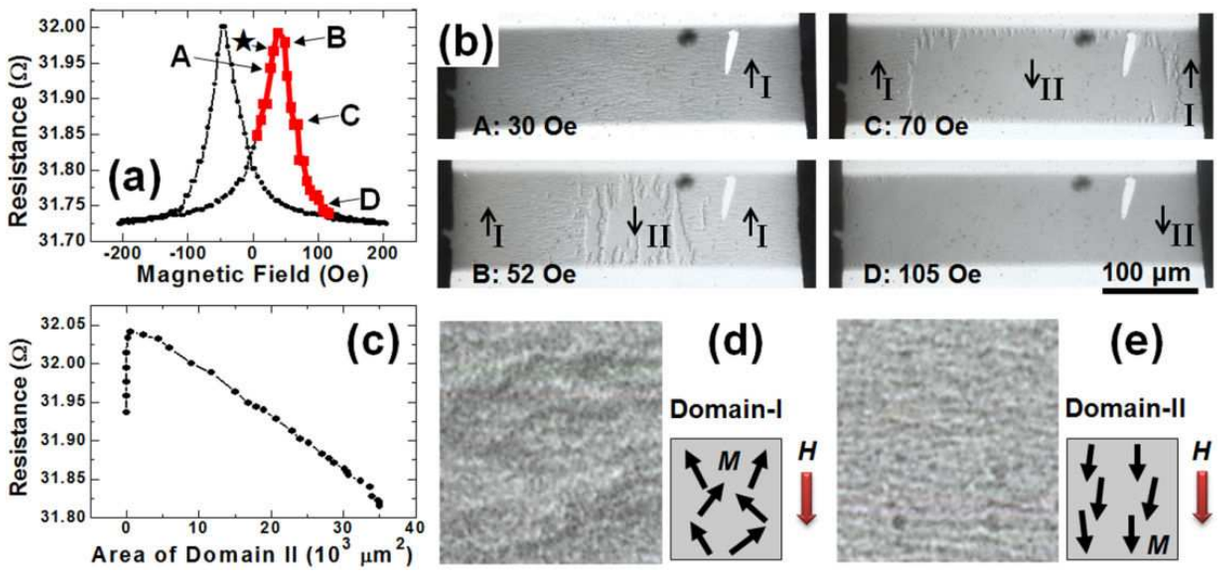

Figure 12. (a) MR curve measured with TEM. Domain wall appeared at point indicated by star. (b) LTEM at A-D in (a) (arrow: averaged direction of *M*). In-plane field *H* was downward in image. Dark regions on both ends of image are voltage terminals. (c) Resistance as a function of area of domain-II. Enlarged images in domains (d) I and (e) II with schematics of local moments (arrows).

The Py pattern was composed of a single domain (domain-I) in the state A (30 Oe), where the average magnetization is upward in the image. Resistance increased monotonically with the field. Domain-II having magnetization parallel to the field (downward) appeared at 43 Oe (state marked with a star in Fig. 12(a)). However, no remarkable changes in resistance could be identified. After this, the area of domain-II monotonically increased with the field. Resistance reached maximum at ~50 Oe, and then reduced monotonically (states B and C). At ~105 Oe (state-D), all regions were composed of domain-II with downward magnetization in the image. While decreased resistance continued after the disappearance of DWs, the rate of reduction was small. The resistance was plotted as a function of the area of domain-II (Fig. 12(c)) to investigate this change. It decreased linearly with this area. It is clear that resistances in domain-I (anti-parallel *M* and *H*) and domain-II (parallel *M* and *H*) differ.

By carefully observing the images in Fig. 12(b), we can identify fine stripe contrast, which is caused by magnetization ripple. This contrast was stronger in domain-I than that in domain-II (Figs. 12(d) and 12(e)). This indicates that the orientation dispersion of the local moment was strong in domain-I, and thus the moment inclined from a direction perpendicular to the current ($\theta < 90°$). However, this dispersion was weak in domain-II, and the moment was almost perpendicular to the sense current ($\theta \sim 90°$). The AMR effect is described as in Eq. 2. Thus, domain-II having weak dispersion should have lower resistance than domain-I. This is a possible explanation for the decrease in resistance in Fig. 12(c). A similar discussion can explain the increase in resistance in regions with small domain-II area. Magnetic domains with magnetization along the applied field have smaller resistance than domains with magnetization opposite to the field.

5.2.2. Experiments by using electromagnet holder

The experimental system is outlined in the schematics in Figs. 1(a), 1(b), 1(d), and Fig. 3. This subsection provides three examples using the electromagnet holder we developed.

5.2.2.1. Domain wall injection and movement in a wire pattern

The control of DWs in magnetic wires has been widely reported [42, 43]. A pad is usually attached to the wire to achieve stable injection of DWs into them [44]. There is a series of LTEM images of a Py wire pattern with a square pad with varying in-plane fields in Fig. 13. A field was applied horizontally. After 100 Oe was applied along the left to saturate magnetization, the field was gradually removed to zero (Fig. 13(a)). The wire was almost uniformly magnetized to the left. The contrast at the lower edge was dark while it was white at the upper edge. There was a clear structure of a solenoidal domain (with 90° and 180° DWs) inside the pad. The area of the domain around the pad's centre penetrated the wire under 6 Oe along the right in Fig. 13(b). A vortex DW (arrowhead) was injected in this case. The contrast of the wire edge changed from the left to the right. The DW moved to the right (Figs. 13(c)–(e)) by increasing the field along the right. The Py pattern was almost saturated in Fig. 13(f). Finally, it was fully saturated in Fig. 13(g) under 100 Oe. The wire edge contrast was reversed from that in Fig. 13(a). Increases and decreases as well as reversal of the magnetic field could be efficiently accomplished by using the system that we developed in this research.

5.2.2.2. Movement of vortex core by field rotation

Ferromagnetic patterns have attracted a great deal of attention in the development of miniaturized memories and logics. Disks with a vortex structure (Fig. 14(a)) represent one such pattern [45, 46]. Local magnetic moments form a clockwise or anti-clockwise loop, and that at the vortex core turns out-of-plane. The vortex core moves perpendicularly to the field when an in-plane field is applied. The direction of movement depends on the chirality of the vortex. There is a test pattern in Fig. 14(b), where Py disks with diameters of 5 and 10 μm can be seen. The arrow denotes an in-plane field of 11 Oe. The bright or dark spotty contrast near the centre of each disk corresponds to a vortex core. The LTEM contrast of the vortex core and disk edge alternates depending on the chirality of the vortex, as shown in Fig. 14(a). A series of LTEM

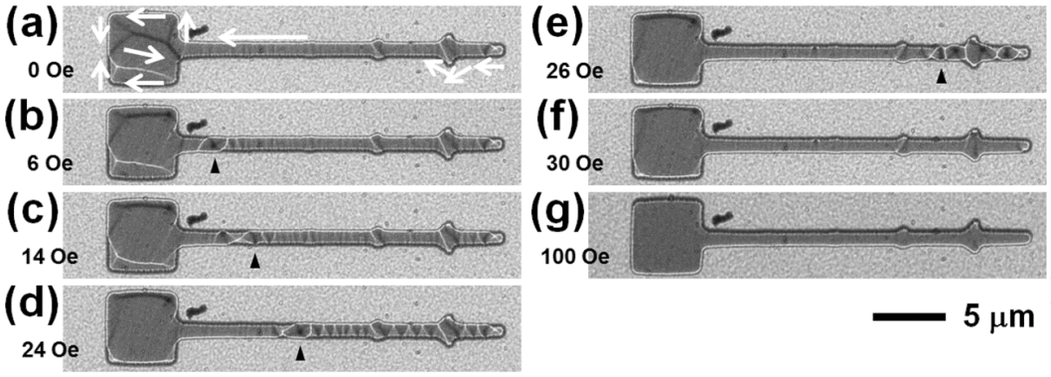

Figure 13. *In situ* LTEM images of Py wire with square pad by applying field along right. Injection of DW and its movement can be seen without large image deformation. White arrows in (a) denote local magnetization. Arrowheads in (b)-(e) indicate DW positions.

images with rotating magnetic fields is shown in Figs. 14(b)-(e). The vortex cores were displaced according to the respective fields to expand the area with magnetization nearly parallel to the field. The core positions moved gradually by rotating the field.

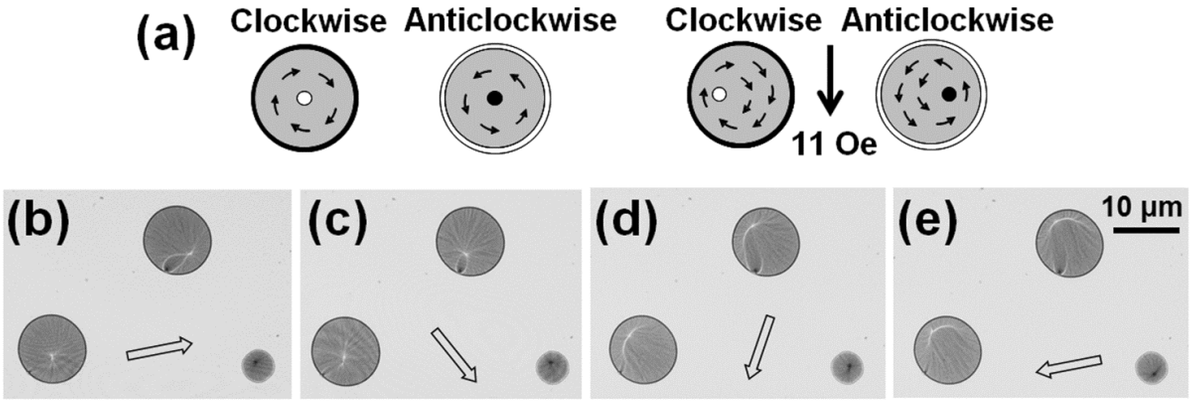

Figure 14. (a) LTEM of thin Py disc patterns with or without magnetic field. (b)-(d) Observed images with rotating in-plane field of 11 Oe. Thick arrows correspond to nominal field directions.

5.2.2.3. In-Situ LTEM observations and magnetoresistance measurements

The investigated MR effect was the longitudinal AMR where resistance was high with magnetization parallel or anti-parallel to the sense current. There is an example of an MR curve measured with TEM in Fig. 15(a), where the magnetic field was parallel to the sense current. Well-known positive MR was identified, where resistance was low around a zero magnetic field. *In situ* LTEM images are presented in Figs. 15(b)-(g), which corresponded to states (b)-(g) in Fig. 15(a). The directions of magnetization were roughly estimated by using faint ripple contrast as a guide (arrows). The region is composed of a single domain in Fig. 15(b) at +14 Oe (along the left) after saturation at +125 Oe. When the field was –21 and –28 Oe (along the right), cross-tie walls can be identified as black and white lines in Figs. 15(c) and 15(d) where resistance

http://dx.doi.org/10.5772/60651

was low. When DWs exited the region, resistance increased (Fig. 15(e)). After this, magnetization was saturated along the right, and the field was reversed. The DWs returned to this region at +22 Oe and resistance decreased (Fig. 15(f)). Resistance increased again when the DW exited from the region (Fig. 15(g)).

The pattern investigated in this work was large, and the DWs were expected to be thick [47]. Thus, the MR effect due to DWs themselves must be quite small. The MR effect identified here was caused by the change in the distribution of local magnetization. As seen in Figs. 15(c), 15(d), and 15(f), local magnetization tends to be parallel (or anti-parallel) to the DW, and its orientation inclines from the sense current. Therefore, the resistance is thought to be small. Another possibility influencing the MR effect is the strength of the magnetic ripple. A domain with anti-parallel magnetization to the applied field had clearer contrast than that with parallel magnetization to the field as was described in Subsection 5.2.1. This indicates that the former domain had larger fluctuations in the orientation of the magnetic moment, and thus the local moment was much more inclined from the sense current providing lower resistance. A similar phenomenon was expected, even though this difference in contrast was not clearly observed in this research because of weak contrast in the image.

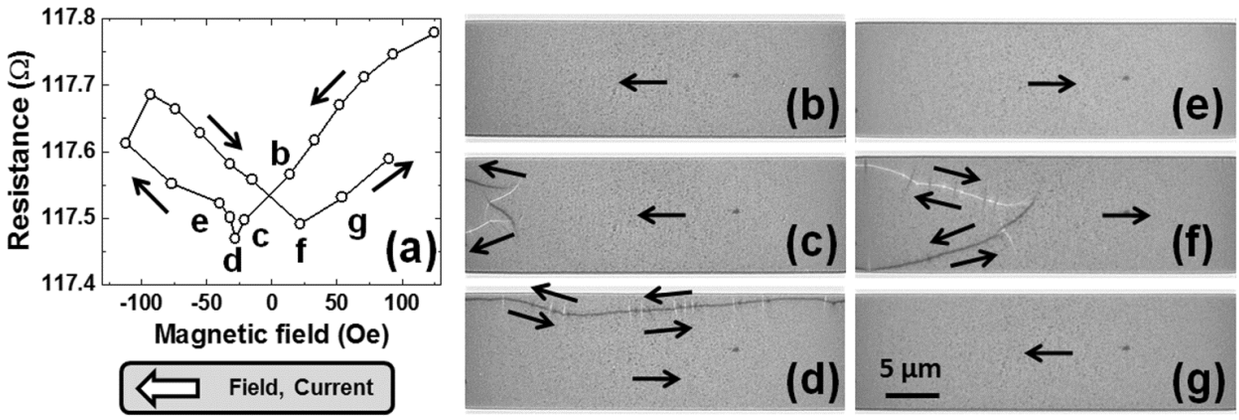

Figure 15. (a) Longitudinal AMR curve of Py pattern measured with TEM (arrow: measurement sequence). (b)-(g) LTEM images of whole area between voltage terminals corresponding to conditions (b) to (g) in (a) (arrow: local orientation of *M*). Magnetic field is positive when it is along left.

5.3. Quantum conductance of metallic nanowires

Metallic contacts and wires on the nanometre scale have been intensively studied [48]. These are expected to exhibit quantum effects at room temperature (RT). Several techniques have been adopted to produce nanowires [49, 50, 51, 52, 53]. Narrow wires with a width of one Fermi wavelength (~0.5 nm) have been the objects, and the energy split of electrons contributes to the conduction quantization.

The quantization unit of conduction in nonmagnetic materials is known to be $2e^2/h$ (= G_0: corresponding resistance is 12.9 kΩ), where e is the electron charge and h is Planck's constant. In ferromagnetic metals where the spin degeneracy is lifted, the quantization step is e^2/h (=

G_0/2). While the nonmagnetic wires such as Au and Cu have mostly exhibited G_0-quantization, a few reports have discussed the G_0/2-quantization [54, 55]. Some possibilities have been revealed to explain this phenomenon, including local atomic arrangement and gas adsorbates [55, 56, 57, 58]. This section explains the formation of Au wires with G_0/2-quantization, and the experimental factors that determined its appearance were investigated [59]. Two Au probes prepared with the method in Figs. 7(a)-(c) were placed inside a TEM, and Au nanowires were formed by touching and detaching these two Au probes. A TEM/STM holder (Fig. 5) was used for this treatment. The system is outlined in Figs. 1(a), 1(c), and 1(e). The TEM was JEM 200CX with a liquid nitrogen trap. The vacuum was 10^{-4}–10^{-5} Pa near the sample and 1–10^{-1} Pa in the pre-evacuation room. The influence of the electron beam was smaller than the current for measurements by two or three orders in magnitude. All measurements were performed at RT.

Three continuous video frames are presented in Figs. 16(a)-(c). The wire length was increased from 4 to 8 nm by stretching it from the state in Fig. 16(a) to that in Fig. 16(b). The wire widths changed from 2 to 1 nm. A further stretch to Fig. 16(c) broke the wire. The corresponding conductance curve is plotted in Fig. 16(d) with a bias voltage (V_b) of 258 mV. A stair-like change can be identified. This conductance quantization was also observed in a process where two probes touched each other. The time interval from $6G_0$ to breakage is ~3 ms, and this curve was obtained between Figs. 16(b) and 16(c). The quantization was observed for a wire having a width of 1 nm or less. Hundreds of curves were usually summarized as a (conductance) histogram. Figure 16(e) is an example using 270 curves having at least one conduction plateau. The experiment was performed with TEM in the Mag-mode (6.5 kOe). The G_0-quantization can clearly be identified. This histogram has also a weak peak at G_0/2. Two conductance with the G_0/2 plateau curves are presented in Figs. 16(f) and 16(g).

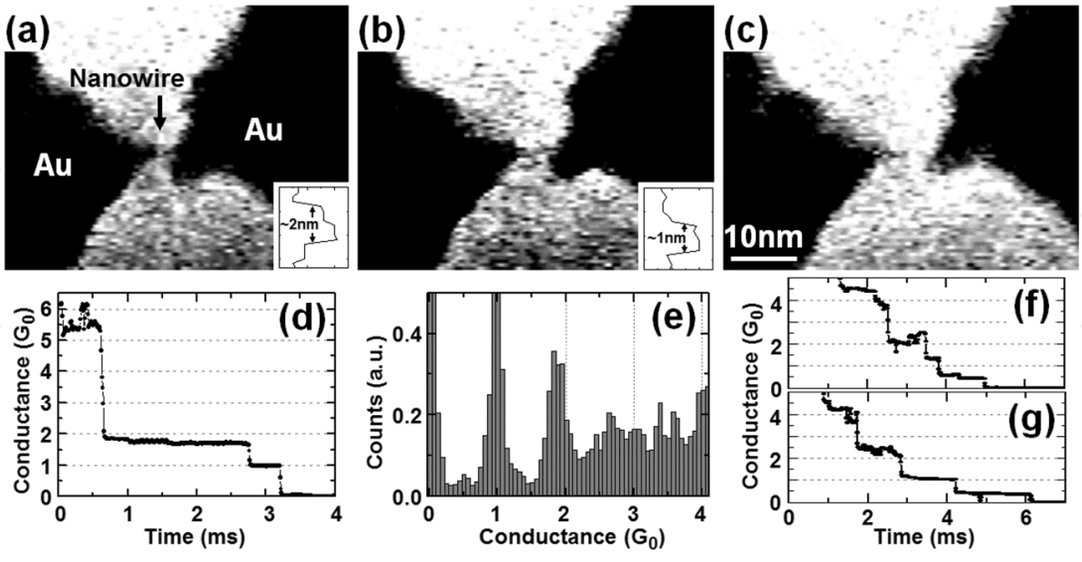

Figure 16. Conductance quantization of Au wires. (a)-(c) Continuous frames of TEM video (interval: 30 ms). Insets are density charts across wire (vertical: magnified vertical position, horizontal: brightness (right: dark)). (d) Conductance curve measured during (a)-(c). (e) Histogram using 270 conductance curves (V_b = 129 mV, H = 6.5 kOe). (f) and (g) Conductance curves having G_0/2 plateau.

http://dx.doi.org/10.5772/60651

Au nanowires were formed under various conditions with different values of H and V_b (Table 1) and the stretching speed (v), to clarify experimental factors influencing the G_0/2-quantization. First, three experiments were carried out at ~6.5 kOe (Mag-mode), ~40 Oe (LowMag-mode), or 0 Oe (samples placed in pre-evacuation room) with V_b = 258 mV. The probability of observing a G_0/2 plateau in the conductance curve was increased from 1% to 8% with increasing the magnetic field. Second, three bias voltages were investigated at ~ 6.5 kOe. The peaks of the conductance histogram broadened by increasing V_b, and the peaks of $2G_0$ and $3G_0$ were weak (data not shown) as in Ref. [50]. Third, a possible effect of the stretching speed (v = 5000, 500, and 5 nm/s) was checked with H = 0 Oe and V_b = 258 mV. The possibilities were 0% (5000 nm/s), 5% (500 nm/s), and 9% (5 nm/s). Previous report (without TEM) that have objected to the G_0/2-quantization revealed that it appeared due to gas adsorption [56, 57, 58]. The present work was carried out under a vacuum of 10^{-5} Pa or worse, and the influence of adsorbates could not be neglected. The following explanation is probable from this standpoint. Heat generation increases with large V_b, and gas molecules tend to desorb. Changes in stretching speed may vary the degree of adsorption. In the first stage of wire formation, Au probes moved against each other and formed the freshly clean wire surface. This wire surface has a chance to be covered with adsorbates during the stretching process. The probability may be high for a slow stretch. The present results, on the other hand, indicated that the probability of G_0/2-quantization increased with magnetic field. This cannot be explained by the direct influence of adsorption such as a partly open conduction channel accompanying any adsorbates or by a conduction circuit of several nano-contacts. One possible scenario that can explain the present results is that the atomic arrangement was modified due to gas adsorption, and that the magnetic properties of the wires were changed due to this modification. As described earlier, G_0/2 conductance is a characteristic of ferromagnetic nanowires where spin degeneracy is lifted. A conductance curve and a histogram of a Fe wire are presented in Fig. 17. Compared with Au wires, G_0/2-quantization can clearly be identified.

Magnetic field H (Oe)	**Bias voltage V_b (mV)**		
	- 26	**- 258**	**- 516**
6500	12%	8%	5%
40	----	3%	----
0	----	1%	----

Table 1. Probability to observe the G_0/2-quantization. The effects of the magnetic field and the bias voltage are summarized.

5.4. Single electron tunnelling of nanoparticle system

The conductance of nanostructures such as SED [11, 12] has been intensively investigated. The miniaturization of current paths plays a key role to observe the quantum effect at RT. An important area of research involves nanoparticle systems embedded in an insulator [60, 61,

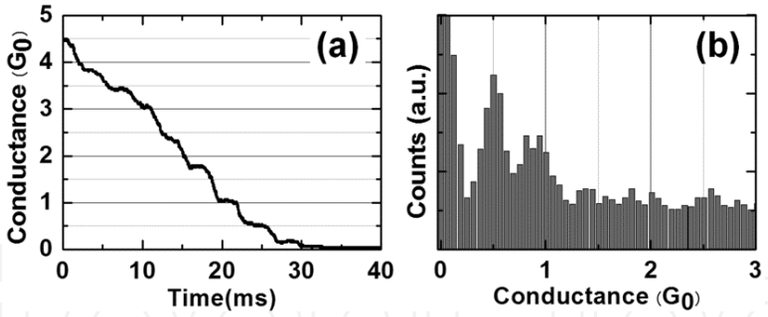

Figure 17. (a) Conductance curve and (b) histogram of Fe wires made from thin Fe layer on sharp Si needle. Measurements were done with TEM in Mag-mode.

62]. The tunnelling current is strongly influenced by their geometric arrangement, such as the particle size (i.e., area of the tunnelling junction) and inter-particle distance (i.e., thickness of the tunnelling barrier).

In this research, the TEM/STM was introduced to investigate the direct relation between the geometry and electrical characteristics of nanoparticle systems. The operation system is outlined in Figs. 1(a), 1(c), and 1(f). The samples were deposited on the needle-shaped Au substrate shown in Figs. 7(c) and 7(d). Two examples are presented, that is, tunnel conduction of a 2-nm thick MgO film and a 5-nm thick MgO/Fe/MgO tri-layer film [8, 29, 63, 64]. Nanoscale regions less than 10 nm^2 were selected using a movable probe. Current-voltage (*I-V*) measurements and TEM observations were performed.

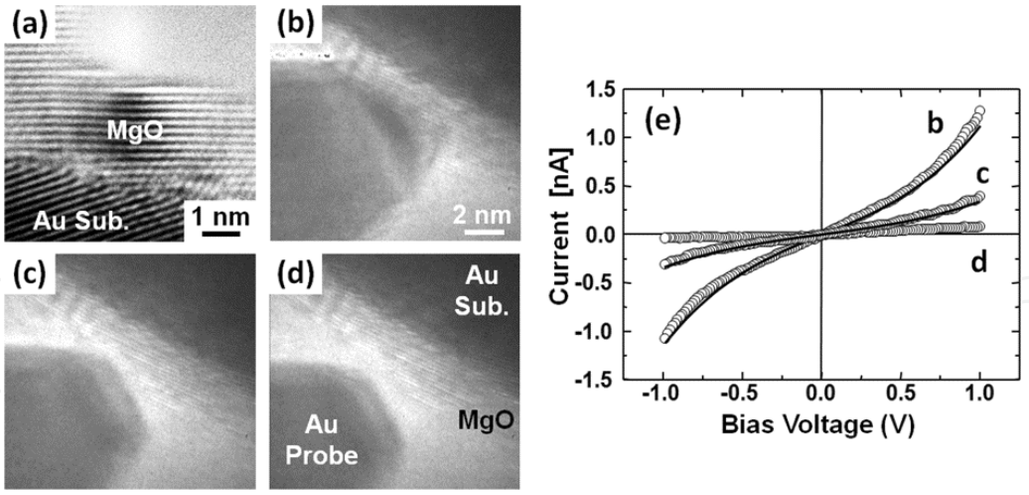

Figure 18. (a) HRTEM image of MgO/Au. (b)-(d) A series of CCD images and (e) corresponding *I-V* curves where solid curves are fitting results obtained by using the Simmons' equation.

There is a typical HRTEM image of MgO/Au with 200_{MgO} and 200_{Au} lattice fringes in Fig. 18(a). The MgO thickness was ~2 nm. Its barrier height for tunnel conduction was evaluated under the conditions in Figs. 18(b)-(d) using *I-V* curves (Fig. 18(e)). First, the probe made contact with the MgO surface. The contact area was ~10 nm^2 (Fig. 18(b)). The corresponding *I-*

http://dx.doi.org/10.5772/60651

V curve indicated nonlinear characteristics in Fig. 18(e). The current was 0.45 nA at V_b = 0.5 V. Next, the probe gradually moved from the sample, and the contact area was reduced. The contact in Fig. 18(c) was ~1.2 nm^2. The current at V_b = 0.5 V decreased to 0.2 nA. The probe was completely separated from the sample in Fig. 18(d), and the background current was measured. Simmons' equation [65] was used to analyse these *I-V* curves to evaluate the barrier height, while this assumption was not rigid because the contact area was not large compared with the MgO thickness.

$$I = \frac{S}{t} \cdot \left(\frac{e}{h}\right)^2 \cdot \sqrt{2m\phi} \cdot \exp\left(-D\sqrt{\phi}\right) \cdot \left\{ V_b + \left(\frac{D^2 e^2}{96\phi} - \frac{De^2}{32\phi\sqrt{\phi}} \right) V_b^{\,3} \right\} \tag{4}$$

and

$$D = 4\pi t \cdot \frac{\sqrt{2m}}{h}. \tag{5}$$

Here, I is the current, S is the contact area, t is the barrier width, ϕ is the barrier height, and V_b is the bias voltage. The constants e, m, and h correspond to the electron charge, the electron mass, and Planck's constant, respectively. Least-square fitting was performed by assuming contact areas described earlier. As a result, ϕ = 1.4 eV was obtained in both cases. This corresponds to the results using conventional tunnel junctions [10, 66].

The following is an example of $MgO_{(2\ nm)}/Fe_{(1\ nm)}/MgO_{(2\ nm)}$, where the Fe layer was composed of nanoparticles (Fig. 19(a)). The film formed a double tunnel junction. As the Fe particle size was on a nanometre scale, the Coulomb blockade (CB) effect was expected at RT. Here, the contact area must be small to detect the quantum effect. Therefore, the sample film was processed inside TEM. After the Au-probe lightly touched the film, 5 V or larger voltage was applied to the probe to exfoliate the sample layer. The narrow current paths were fabricated by repeating this process. Three Fe particles (diameters: 3.4, 3.2, and 2.9 nm) are seen in Fig. 19(b). The particle with a diameter of 2.9 nm was selected for the measurements. The distance between the film surface and the particle was estimated to be 2.4 nm from this image, and the distance between the particle and the Au-sub was 0.8 nm.

The results are presented in Figs. 19(c)-(e), where the tri-layer film can be identified as faint contrast on the Au-sub. The probe softly touched the sample in Fig. 19(c). The tunnelling current in the *I-V* curve was small because of the long probe-particle distance (2.4 nm). The probe was next moved along the white arrow by 1.3 nm to press the sample (Fig. 19(d)). The probe-particle distance was estimated as 1.1 nm by assuming that the Fe-particle positions did not change. This was almost the same as the substrate-particle distance (0.8 nm). The current increased markedly and the *I-V* curve revealed nonlinear characteristics. The current was small with low V_b, although the leakage current seemed to be superposed. This may have been due to the CB effect. The tip was shortly detached from the sample by 0.5 nm in Fig. 19(e). The

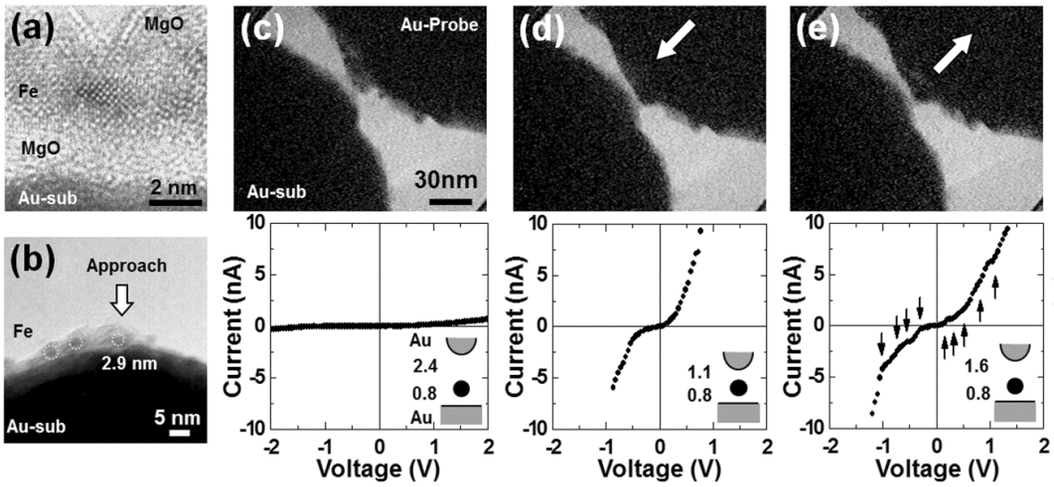

Figure 19. (a) Side view of MgO/Fe/MgO containing Fe particles. (b) Sample used for measurements. (c)-(e) Video images and *I-V* curves during deformation by moving Au probe along arrows (at RT). Steps (arrows) are recognized in *I-V* graph in (e). Insets are schematics of Fe particle (filled circle) sandwiched between Au probe and substrate. Numbers are distances in nm.

current was suppressed. There are weak steps at the positions indicated by the arrows in the *I-V* curve, which are thought to represent the Coulomb staircase (CS). Under this condition, the probe-particle distance was expected to be 1.6 nm while the particle-substrate distance was 0.8 nm (inset of Fig. 19(e)). Therefore, the probe-particle and particle-substrate tunnelling resistances must differ much. This corresponds to a well-known phenomenon that the CS appears only when the resistances of two junctions sandwiching the nanoparticle differ much [11, 12]. The step period was ~0.25 V. The Fe particle in this experiment was sandwiched between two large electrodes (i.e., the probe and substrate). The capacitance C in this nanostructure was assumed to be half the self-capacitance of particle $C_s = 4\pi\varepsilon_0\varepsilon_r r$, where ε_0 is the dielectric constant of the vacuum, ε_r is that of MgO, and r is the radius of the particle. The self-capacitance is $C_s = 1.3$ aF by using $2r = 2.9$ nm and $\varepsilon_r = 9.65$. The CS period is $e/C = 2e/C_s = 0.25$ V. This value approximately fits that obtained from the experimental result.

5.5. Resistance switching of the resistive random access memory

Resistive random access memory (ReRAM) has attracted a great deal of attention as a next-generation non-volatile memory [14, 15, 67, 68, 69, 70]. Its advantages include high-speed operation, low power consumption, etc. High integration is also expected due to its simple capacitor structure (Fig. 20(a)). Resistance switches between high and low resistance states (HRS and LRS) by applying voltage between top and bottom electrodes (TE and BE). The *I-V* curve exhibits hysteresis (Figs. 20(b)-(c)) that is useful in non-volatile ReRAMs. The resistance ratios of HRS/LRS are generally more than 100, and ReRAM devices are expected to be regulated in intermediate states to realize non-volatile analogue memories.

The pristine state is typically HRS and converts into LRS due to the first application of voltage. This process is called "forming". Subsequent voltage returns the resistance into HRS ("reset" process). Resistance again changes into LRS by another application of voltage ("set" process).

http://dx.doi.org/10.5772/60651

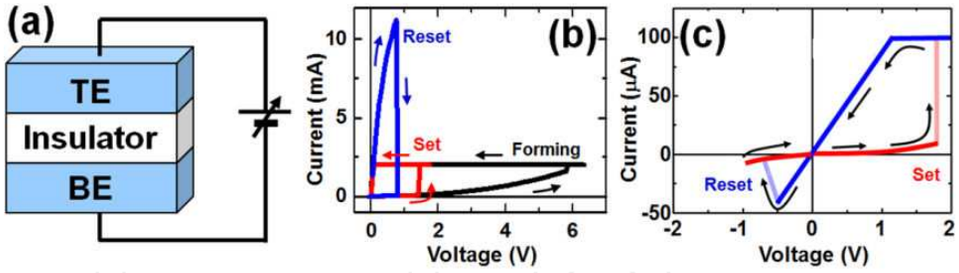

Figure 20. (a) Schematic of ReRAM. *I-V* switching curve of (b) unipolar and (c) bipolar ReRAMs (arrows: sequence of voltage sweep). Horizontal axis denotes setting voltage of SMU.

There are two types of switching. The same voltage polarity is used in "unipolar" switching (Fig. 20(b)), while polarity needs to be altered in "bipolar" switching (Fig. 20(c)). Current abruptly increases during forming or set, and ReRAMs are easily destroyed. To prevent this failure, current limitation (or compliance) of the electrical source is generally introduced. The horizontal line in the *I-V* curve is due to these limitations. Many materials have been applied to ReRAMs [14, 15], and various switching models have been reported. Of these, the "filament model" is believed to play a key role in many cases, where formation and erasure of conductive filaments of oxygen vacancies or Cu contribute to switching. However, their detailed behaviour is still obscure while finding the mechanism is quite important to develop ReRAM devices. *In situ* TEM was carried out in this report by using TEM /STM holders (Fig. 5). The system was that in Figs. 1(a), 1(c), and 1(f). ReRAMs of PtIr/NiO/PtIr [34, 71], PtIr/Cu-GeS/PtIr [72, 73], and Cu/MoO_x/TiN [74, 75, 76] will be explained.

5.5.1. Unipolar switching of PtIr/NiO/PtIr

A binary oxide NiO is one of the most widely investigated materials for ReRAMs and exhibits unipolar switching. The mechanism for this switching phenomenon may be one of the filament models based on soft-breakdown [68]. A conductive filament of oxygen vacancies connecting metal electrodes is formed during the forming. This forming process certainly plays a key role in achieving stable switching cycles. In this study, sharp PtIr probes (tip size: several tens of nanometres or less) to obtain *I-V* data from nano-regions were used, which were sharpened using the methods in Figs. 7(a) and 7(e). Wedge-shaped PtIr substrates (Figs. 7(f)-(h)) were used to deposit NiO. The Ni metal was deposited at RT onto this substrate, and oxidation was performed in air for 3 min typically at 200°C or 300°C. The NiO layer (40–50 nm in thickness) was polycrystalline with a grain size of 30–50 nm. The size of the apex of the probe was comparable to or less than this grain size, and thus the *I-V* characteristics could be obtained from individual grains. Because forming operation based on soft-breakdown is more or less violent, the films were permanently destroyed in many cases. Therefore, a resistor of 10 kΩ was inserted in series in the circuit to prevent this destruction.

The *I-V* curve is plotted in Fig. 21(a), and the corresponding TEM micrographs are in Figs. 21(b) and 21(c). The probe was moved along the arrow to make electrical connection with the NiO layer (Fig. 21(b)). The contact area was ~1200 nm^2 or less. The conducting properties were measured through this point. The voltage sweep sequence was typically from 0 to 3 V and

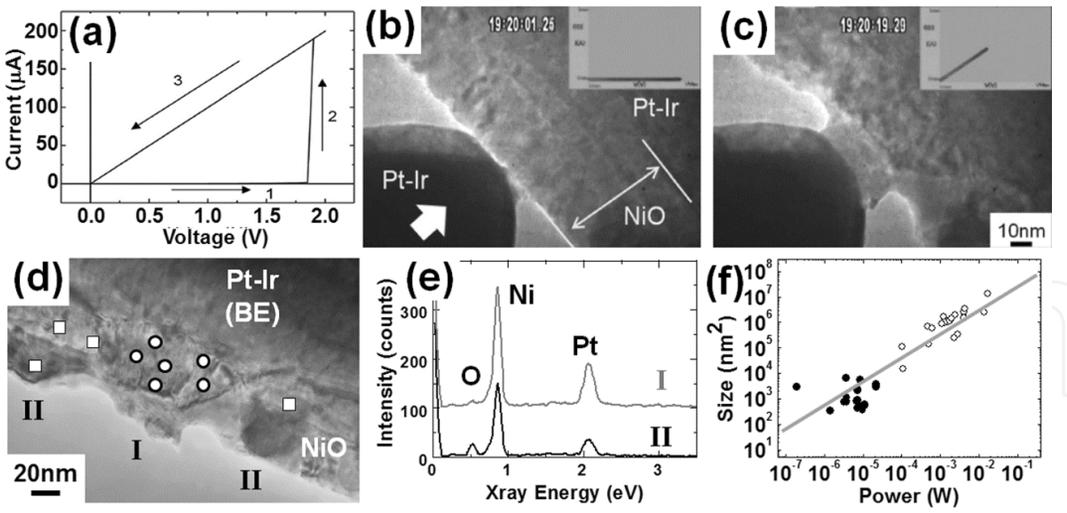

Figure 21. ReRAM switching of PtIr/NiO/PtIr in TEM. (a) *I-V* characteristics. Corresponding TEM micrographs (b) before and (c) after forming. (d) Image of filament in (c) after TE probe was detached. There is wreck of filament at centre (I, circles), which was surrounded by initial NiO (II, square). energy dispersive X-ray spectroscopy (EDX) was performed at these positions. (e) EDX spectra from regions I and II. (f) Filament size (filled circles) superposed on CS size (open circles). Line is extrapolation from CS data.

back to 0 V. The measurements were done within 18 seconds in which drift in the electrodes could be neglected. The current hardly passed in the first sequence (sequence 1), and the TEM image remained unchanged (Fig. 21(b)). Resistance (R) was ~1 MΩ. When voltage was increased to 1.7 V, the current suddenly increased (sequence 2) and the NiO film structure changed to have a bridge-like contrast (Fig. 4(b)). When the voltage was decreased to 0 V (sequence 3), resistance was almost that of the series resistor (10 kΩ). NiO changed to LRS (R <<10 kΩ). The PtIr electrode was then detached and touched again. R in region I of Fig. 21(d) (filament position) was still in LRS while adjacent region II remained insulating. The bridge region worked as a conductive filament. Regions I and II were analysed by using energy dispersive X-ray spectroscopy (EDX) at the positions with circles and squares in Fig. 21(d). Typical spectra are compared in Fig. 21(e). The oxygen peak was apparently weakened in region I. The estimated composition of Ni: O was 71: 29 for region I and 85: 15 for region II. This finding fits with the phenomenon in the filament model of binary oxides where the redox reaction contributes to switching. The forming power and the filament size are also important factors. Crater-shaped "conduction spots" (CS) have been observed using conventional ReRAM samples, and the CS area was proportional to the injection power [77]. The filament diameter measured from TEM images are summarized (filled circles) in Fig. 21(f) where the CS data are superposed as open circles. The bridge size was ~300 nm^2 (~20 nm diameter) at 10^{-6} W, and the size is expected to be less than 100 nm^2 (~ϕ12 nm diameter) at ~10^{-7} W. This indicates there is great potential in the scaling of resistive switching.

While the filament formation during the forming process could clearly be identified, reset operation was not found in TEM where the ambient was a vacuum. We fabricated NiO/Pt on a SiO_2/Si substrate which was not a TEM sample, to investigate the reason for this result. The *I-V* measurements (data are not provided here) were performed in air and in a vacuum by

using a PtIr probe as the TE. The switching sequence of the forming-reset-set was identified when the PtIr/NiO interface was exposed to air. However, there was no reset in the vacuum. After the vacuum was broken, reset-set operation recovered. Therefore, the phenomenon that appeared during *in situ* TEM experiments could be understood as follows. Oxygen in NiO diffused into the vacuum in the forming process, and did not remain in the vicinity of the PtIr/NiO interface. Therefore, the conductive filament could not be oxidized, and the reset process could not be achieved. Oxygen and/or water vapour played an important role in the ReRAM switching of NiO.

5.5.2. Bipolar switching of PtIr/Cu-GeS/PtIr

The ReRAMs of solid electrolytes are other examples (e.g., CuGeS and Ag_2S) [14, 67, 69]. This type of ReRAM is abbreviated as CBRAM (conductive bridging RAM) as well as PMC (programmable metallization cell). The operation is attributed to the conductive filament of Cu (or Ag). The cations (e.g., Cu^{2+}) generated at the anode are thought to migrate toward the cathode with bias voltage. The cations receive electrons at the cathode surface and become metal atoms. Metallic filament is formed by continuing this process, and it bridges the cathode and anode. An opposite bias voltage dissolves the metallic filaments into the solid electrolyte. This is the expected switching process. Real-space *in situ* observations are quite effective to elucidate this hypothesis and provide further detailed information. Cu-GeS thin films were deposited on the PtIr substrate. The films were 8–60 nm thick and were amorphous including Ge nanocrystals. The Cu ion source was the Cu-GeS layer itself. Although amorphous chalcogenides easily deteriorated during TEM observations, the influence of the electron beam was negligible (beam current densities lower than 170 fA/nm^2). A sharp PtIr probe was used as the TE. Since the substrate and the probe had different shapes, the structure of PtIr/Cu-GeS/PtIr was asymmetric while it was electrochemically symmetric.

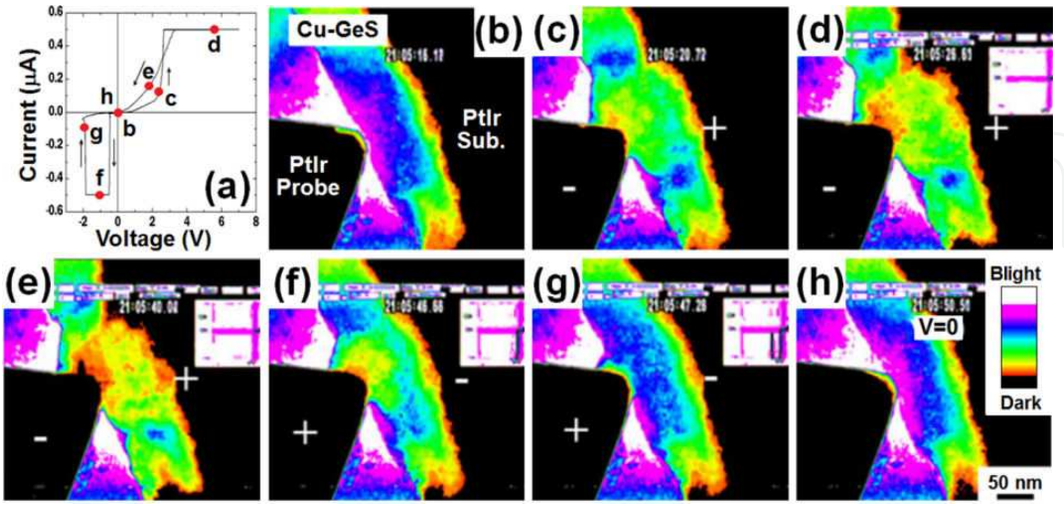

Figure 22. ReRAM switching of PtIr/Cu-GeS/PtIr in TEM. (a) *I-V* characteristics measured with TEM. (b)-(h) Series of images during application of voltage. Conductive filament in red and yellow appeared from the probe side (grounded) and disappeared during switching process.

The *I-V* curve during the *in-situ* TEM observations is plotted in Fig. 22(a), where the substrate was biased with the current compliance of 0.5 μA. The voltage was swept from 0 to 7 V, from 7 to –2 V, and back to 0 V, which indicates hysteresis. TEM images in pseudo-colours are presented in Figs. 22(b)-(h). The red and yellow parts correspond to dark contrast in the original images (Fig. 22(h)). There was no special contrast just after the probe contacted Cu-GeS (Fig. 22(b)). The resistance gradually changed at ~1 V, and this transfer was quickly completed at 2.6 V. This was the set operation. A small deposit (green, yellow, and red) gradually appeared in the same way (Fig. 22(c)). The size of the deposit was enlarged (Figs. 22(d)-(e)) and it contacted the substrate. The width of the filament-like red region was 10 nm. Although the details were altered by colouring conditions, this value may give some insights into the filament size. The *I-V* curve between (d) and (f) of Fig. 22(a) was abnormal compared with the curves of usual ReRAMs. Resistance suddenly increased at –0.5 V. This was caused by over accumulation of Cu around the TE (i.e., probe). This specially occurred for the sample without the Cu substrate and is not the set or the reset. The mechanism has been discussed in Ref. [73]. The deposit contracted as the application of negative voltage continued (Figs. 22(f)-(g)), and the sample resistance returned to HRS. This was reset switching. The deposit entirely disappeared in Fig. 22(h). The size of the deposit and the current value corresponded, and the deposit constituted a conducting path. The dependence on polarity may be attributed to the asymmetry of electric field caused by the difference in shape between the substrate and the probe. When positive voltage was applied to the substrate, Cu ions accumulated at the probe because of the concentrated electric field. However, when negative voltage was applied to the substrate, electric flux dispersed toward the substrate. Even though Cu was thought to accumulate at the substrate–film interface, its density was not high enough to form the filament connecting electrodes.

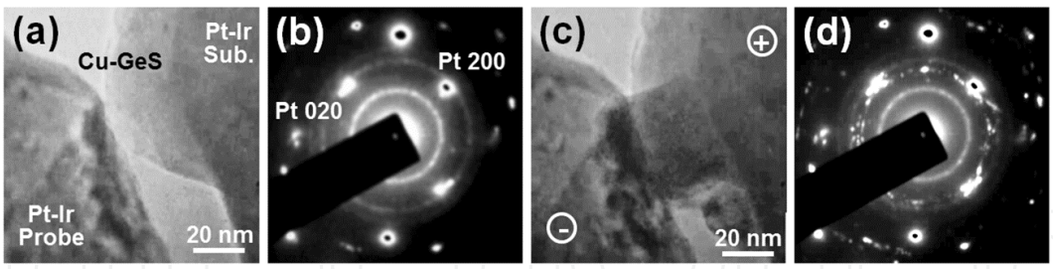

Figure 23. TEM micrograph and corresponding SAD pattern extracted from video (a) and (b) before and (c) and (d) during application of voltage (1 V).

The crystal structure of the deposit was studied by observing real-time selected area diffraction (SAD) patterns. The SAD pattern before voltage application was composed of a faint background and Debye rings (Figs. 23(a) and 23(b)), which indicated the film was amorphous with Ge nanocrystals. The clear spots were from PtIr. A deposit appeared by applying 1 V to the substrate (Fig. 23(c)), and sharp spots appeared in the SAD pattern. They continued to twinkle when voltage was applied. Well-crystallized nanocrystals grew, and their orientation frequently changed. We superposed 1152 frames of video images totalling 35 seconds of footage (Fig. 23(d)). Relatively sharp spots that formed rings corresponded to reflections of Cu. EDX

spectra were measured from the filament and other regions (but another sample). The intensity of the Cu peak greatly increased in the filament region. The composition of the deposit was Cu: Ge: S = 7: 2: 1 while it was 4: 4: 2 in the initial state by assuming thin foil approximation. Although this was a rough estimation, we can summarize that the deposit was an agglomeration of crystals with a large amount of Cu.

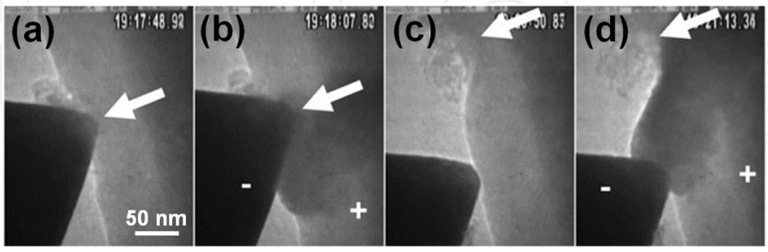

Figure 24. TEM images of (a) and (b) first, and (c) and (d) second switching from initial state (arrows: corresponding position). (a) and (c) are without voltage while (b) and (d) are with voltage of 5 V.

The sample after the voltage cycle differed from its initial state. Continuation of the *I-V* cycles reduced the set voltage. After a deposit appeared and was erased in the first voltage cycle (Figs. 24(a) and 24(b)), the contact position moved to a neighbouring region (Fig. 24(c)). A deposit appeared by applying positive voltage to the substrate (Fig. 24(d)). The deposit did not reach the substrate near the probe but elongated into the region where it had formed during the first cycle. The deposit appeared in the same place in iterative measurements. The regions where the deposit had been formed were thought to have priority in resistance switching. Extremely small metallic nanocrystals or clusters may have remained as residues, which could act as the nuclei of filaments and reduce the set voltage.

The phenomenon that occurred here can be explained in Fig. 25. An electric field is generated by applying positive voltage to the substrate, and the Cu ions dispersing in Ge-S move to the probe. Then, a small metallic deposit appears at the probe (Fig. 25(a)). The deposit expanded and finally touched the substrate (Figs. 25(b)-(c)). At this stage, the conductive filament bridges the probe and the substrate, and the resistance state is LRS. When further voltage is applied, several filaments increase even though the overall size of the conductive region does not expand (Fig. 25(d)). The Cu-based filaments dissolve and shrink toward the probe due to polarity change (Figs. 25(e)-(f)), and resistance reverts to HRS. There are some residues (nuclei of filaments) at the end of the cycle.

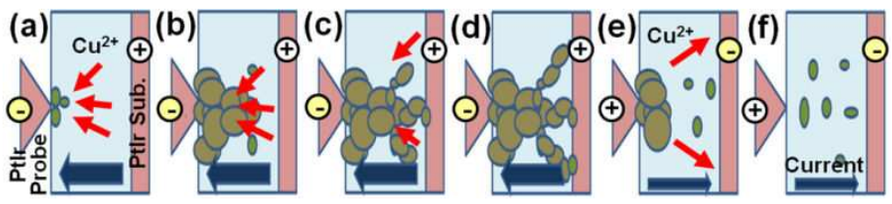

Figure 25. Schematic of resistance switching. Plus and minus signs indicate voltage polarity.

5.5.3. Formation and erasure of conductive filament in Cu/MoO$_x$/TiN

In situ TEM has successfully applied on ReRAM switching [34, 72, 78, 79, 80]. However, the sample was specially designed for TEM observations. For example, the TE was the movable probe. This structure was different from that of real ReRAM devices having multi-layered stacks. In addition, operation was quite slow, and the current was much less than a few μA. The ReRAM studied here was $Pt_{(100\ nm)}/Cu_{(30\ nm)}/MoO_{x\ (50\ nm)}$ on a TiN/Si substrate. The amorphous MoO_x (x ~ 3) acted as the switching layer [81, 82]. Samples were prepared using the ion-shadow method. Clear stacking images were obtained by using the double tilt TEM/STM holder (Fig. 8(f)). After the probe had been connected to the Pt layer, bias voltage was applied to Pt/Cu, and the substrate was grounded. The voltage was typically swept between ±3.0 V (rate: 0.7–0.8 V/s). The switching layer was nearly a disk with ϕ350 nm.

There is an example of the *I-V* curve (compliance current I_c = 400 μA) in Fig. 26(a). The current gradually increased and then abruptly jumped to I_c at 2.6 V (C, set) by increasing the positive voltage (Cu TE biased) from A to B. After positive voltage changed to D and E, it was reduced to zero. The polarity was reversed after 5 minutes. The resistance was LRS. The current exhibited two small jumps before G (reset to HRS). Negative current reached –400 μA with increasing the negative voltage to –3 V (G to H), and clear hysteresis characteristics were identified. The voltage was set to zero. This cycle denoted bipolar switching. The property of this *I-V* curve measured with TEM agreed well with that of ReRAM devices, and thus the vacuum environment and electron beam irradiation had no negative effects.

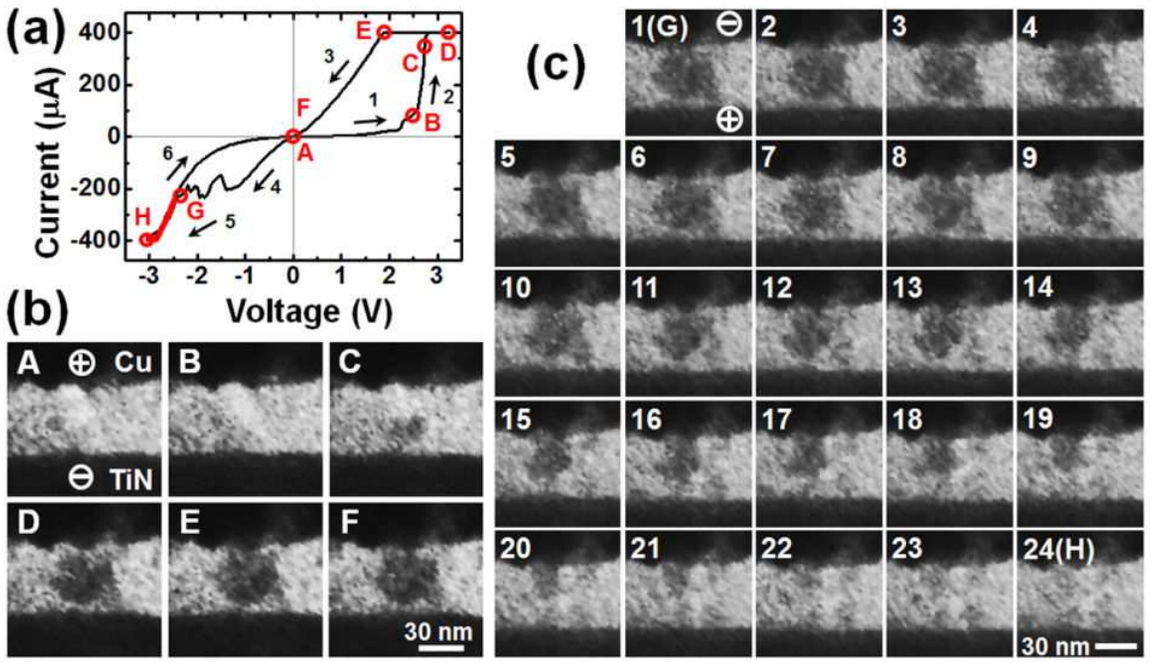

Figure 26. ReRAM switching of Cu/MoO$_x$/TiN multilayer where voltage was applied to Cu TE. (a) *I-V* curve during *in situ* observation. Alphabetical symbols correspond to images in (b) and (c). Magnified filament images in (b) set process and (c) reset process, which were extracted from the video. Numbers indicate the order of video frames counted from G (interval: 30 ms).

Filament-like dark contrast appeared in the set process and disappeared in the reset process. This indicates that this dark region behaved as a conductive filament. We analysed it (but in another sample) with EDX and found it contained more Cu than the other regions. Filament images extracted from the video of the set process (A to F) are summarized in Fig. 26(b). No drastic changes in the images can be identified between A and B (HRS). However, a small dark contrast appeared near TiN BE during abrupt set switching, which seemed to be the nucleus of the filament. Even though the current almost reached I_c at C, the filament did not connect to Cu TE. The current may be ionic that was contributed due to movements of dense Cu ions between the filament and TE. The filament grew toward Cu TE until D, and it thickened to be ~35 nm. After the nucleus appeared, the filament bridged two electrodes within 200 ms. This fits well with the electrochemical switching model [14, 69, 73].

The resistance change in the reset process was gradual. Even after the two-step weak reset, image G (frame #1) had similar contrast to F while resistance increased (Fig. 26(c)). The reset switching should occur very locally (e.g., at the ends of filaments). When we further increased the negative voltage to –2.6 V, negative current increased beyond –300 μA (#12), and the filament shrank toward Cu TE. When the current reached $-I_c$, the filament vanished although some residuals remained (H: #24). This filament erasure does not fit with reported models [83, 84]. This may be influenced by the surface oxidation of TiN BE. This region must have had higher resistance than other regions in the filament and generated Joule heat. This Joule heat must affect filament shrinkage, since it occurred at a relatively high current.

6. Summary and conclusion

We have shown various TEM holders developed in our group in the last 15 years. These holders can be used as accessories without changing the construction of the electron microscope. Thus, their principal design can be applied to any microscopes. In this paper, application of *in situ* TEM holders on magnetic and electronic devices was demonstrated, which are operated by voltage or current input. While some of these TEM holders have already been taken to the market, the designing and manufacturing of new TEM holders is still important for *in situ* TEM experiments for electronics because required functions of the holder depends on devices investigated.

Acknowledgements

This work was financially supported by KAKENHI, by the Ministry of Education, Culture, Sports, Science and Technology (MEXT) Japan, and by the Japan Society of the Promotion of Science (JSPS) (Nos. 13650708, 16206038, 17201029, 18560640, 19026001, 20035001, 21560681, 22240022, 24360128, 25420279, and 26630141). Part of this work was collaborated with the Semiconductor Technology Academic Research Center (STARC), as well as Prof. S. Takeda (Osaka Univ.) under the Cooperative Research Program of "Network Joint Research Center

for Materials and Devices". Support by the Nanotechnology Platform Program (Hokkaido Univ.) organized by MEXT, especially by Prof. N. Sakaguchi (Hokkaido Univ.), is grateful. We are thankful to Dr. T. Tesfamichael (Queensland Univ. Technol.) for critical reading of the manuscript. Finally, we are also grateful to our laboratory members for collaboration.

Author details

Masashi Arita[1*], Kouichi Hamada[1], Yasuo Takahashi[1], Kazuhisa Sueoka[2] and Tamaki Shibayama[3]

*Address all correspondence to: arita@nano.ist.hokudai.ac.jp

1 Laboratory of Nanomaterial Engineering, Graduate School of Information Science and Technology, Hokkaido University, Sapporo, Japan

2 Laboratory of Nanoelectronics, Graduate School of Information Science and Technology, Hokkaido University, Sapporo, Japan

3 Center for Advanced Research of Energy and Materials, Graduate School of Engineering, Hokkaido University, Sapporo, Japan

References

[1] Hirsch PB, Howie A, Nicholson, Pashley DW, Whelan MJ. Electron Microscopy of Thin Crystals. London: Butterworths; 1965.

[2] Fuchs VE, Liesk W. Optik. 1962; 19(6):307-310, in German.

[3] Blech IA, Meieran ES. J. Appl. Phys. 1969; 40(2):485-491.

[4] Iwatsuki M, Murooka K, Kitamura SI, Takayanagi K, Harada Y. J. Elect. Microsc. 1991; 40(1):48-53.

[5] Kizuka T, Yamada K, Deguchi S, Naruse M, Tanaka N. Phys. Rev. B. 1997; 55(12): R7398-R7401.

[6] Poncharal Ph, Frank St, Wang ZL, de Heer WA. Eur. Phys. J. D. 1999; 9(1):77-79.

[7] Svensson K, Jompol Y, Olin H, Olsson E. Rev. Sci. Instr. 2003; 74(11):4945-4947.

[8] Hirose R, Arita M, Hamada K, Takahashi Y, Subagyo A. Japn. J. Appl. Phys. 2005; 44(24):L790-L792.

[9] Miyazaki T, Yaoi T, Ishio S. J. Magn. Magn. Mater. 1991; 98(1):L7-L9.

[10] Yuasa S, Nagahama T, Fukushima A, Suzuki Y, Ando K. Nature Mater. 2004; 3(12): 868-871.

[11] Grabert H, Devoret MH, editors. Single Charge Tunneling. New York: Springer; 1992.

[12] Takahashi Y, Ono Y, Fujiwara A, Inokawa H. J. Phys. Cond. Matter. 2002; 267(14):R995-R1033.

[13] Liu SQ, Wu NJ, Ignatiev A. Appl. Phys. Lett. 2000; 76(19):2749-2851.

[14] Waser R, Aono M. Nat. Mater. 2007; 6(11):833-840.

[15] Akinaga H. Japn. J. Appl. Phys. 2013; 52(10R):100001.

[16] Park H, Lim AKL, Alivisatos AP, Park J, McEuen PL. Appl. Phys. Lett. 1999; 75(2): 301-303.

[17] Heersche HB, Lientschnig G, O'Neill K, van der Zant HSJ, Zandbergen HW. Appl. Phys. Lett. 2007; 91(7):072107.

[18] Strachan DR, Johnston DE, Guiton BS, Datta SS, Davies PK, Bonnell DA, Johnson ATC. Phys. Rev. Lett. 2008; 100(5):056805.

[19] Murakami Y. Real-time investigation of the electrically-induced metal atom migration by use of transmission electron microscopy [thesis]. Sapporo: Hokkaido Univ. 2015, in Japanese.

[20] Chapman JN, Scheifein MR. J. Magn. Magn. Mater. 1999; 200(1):729-740.

[21] Haug T, Vogl A, Zweck J, Back CH. Appl. Phys. Lett. 2006; 88(8):082506.

[22] Shindo D, Akase Z. Kenbikyo(Microscopy). 2009; 44(1):35-40, in Japanese.

[23] Hamada K, Chimura M, Arita M, Ishida I, Okada A. J. Elect. Microsc. 1999; 48(5): 595-600.

[24] Uhlig T, Heumann M, Zweck J. Ultramicros. 2003; 94(3-4):193-196.

[25] Inoue M, Tomita T, Naruse M, Akase Z, Murakami Y, Shindo D. J. Elect. Microsc. 2005; 54(6):509-513.

[26] Petford-Long AK, Bromwich T, Kohn A, Jackson V, Kasama T, Dunin-Borkowski R, Ross CA. Mater. Res. Soc. Symp. Proc. 2006: p. 907E, 0907-MM04-01.

[27] Yi G, Nicholson WAP, Lim CK, Chapman JN, McVitie S, Wilkinson CDW. Ultramicrosc. 2004; 99(1):65-72.

[28] Arita M, Tokuda R, Hamada K, Takahashi Y. Mater. Trans. 2014; 55(3):MD201310.

[29] Arita M, Okubo Y, Hamada K, Takahashi Y. Superlat. Microstr. 2008; 44(4-5):633-640.

[30] Jacobs JWM, Verhoeven JFCM. J. Microsc. 1986; 143(1):103-116.

[31] Khamsehpour B, Wilkinson CDW, Chapman JN, Johnston AB. J. Vac. Sci. Technol. B. 1996; 14(5):3361-3366.

[32] Takezaki T, Yagisawa D, Sueoka K. Japn. J. Appl. Phys. 2006; 45(3B):2251-2254.

[33] Hirose R, Arita M, Hamada K, Okada A. Mater. Sci. Eng. C. 2003; 23(6-8):927-930.

[34] Fujii T, Arita M, Hamada K, Kondo H, Kaji H, Takahashi Y, Moniwa M, Fujiwara I, Yamaguchi T, Aoki M, Maeno Y, Kobayashi T, Yoshimaru M. J. Appl. Phys. 2011; 109(5):053702.

[35] Kudo M, Arita M, Ohno Y, Fujii T, Hamada K, Takahashi Y. Thin Solid Films 2013; 533:48-53.

[36] Black JR. Proc. 6th Ann. Reliability Phys. Symp. 6-8 Nov. 1967 ; Los Angels, CA, USA. New York: IEEE; 1967. p. 148-159.

[37] Park J, Pasupathy AN, Goldsmith JI, Chang C, Yaish Y, Petta JR, Rinkoski M, Sethna JP, Abruna HD, McEuen PL, Ralph DC. Nature. 2002; 417(6890):722-725.

[38] Suga H, Horikawa M, Odaka S, Miyazaki H, Tsukagoshi K, Shimizu T, Naitoh Y. Appl. Phys. Lett. 2010; 97(7):073118.

[39] Chen LJ, Wu WW. Mater. Sci. Eng. R. 2010; 70(3-6):303-319.

[40] Arita M, Hamada K, Ono T, Okada A. Trans. Magn. Soc. Japn. 2004; 4(1):9-12.

[41] Michita N, Arita M, Hamada K, Takahashi Y. J. Magn. Soc. Japn. 2005; 29(2):128-131, in Japanese.

[42] Allwood DA, Xiong G, Faulkner CC, Atkinson D, Petit D, Cowburn RP. Science. 2005; 309(5741):1688-1692.

[43] Parkin SSP, Hayashi M, Thomas L. Science. 2008; 320(5873):190-194.

[44] Cowburn RP, Allwood DA, Xiong G, Cooke MD. J. Appl. Phys. 2002; 91(10): 6949-6951.

[45] Miramond C, Fermon C, Rousseaux F, Decanini D, Carcenac F. J. Magn. Magn. Mater. 1997; 165(1-3):500-503.

[46] Pigeau B, de Loubens G, Klein O, Riegler A, Lochner F, Schmidt G, Molenkamp LW, Tiberkevich VS, Slavin AN. Appl. Phys. Lett. 2010; 96(13):132506.

[47] Fuller HW, Hale ME. J. Appl. Phys. 1960; 31(2):238-248.

[48] Agraït N, Yeyati AL, van Ruitenbeek JM. Phys. Rept. 2003; 377(2-3):81-279.

[49] Pascual JI, Méndez J, Gómez-Herrero J, Baró AM, García N, Binh VT. Phys. Rev. Lett. 1993; 71(12):1852-1855.

[50] Yasuda H, Sakai A. Phys. Rev. B. 1997; 56(3):1069-1972.

[51] Shu C, Li CZ, He HX, Bogozi A, Bunch JS, Tao NJ. Phys. Rev. Lett. 2000; 84(22): 5196-5199.

[52] Ohnishi H, Kondo Y,Takayanagi K. Nature. 1998; 395(6704):780-783.

[53] Kizuka T, Umehara S, Fujisawa S. Japn. J. Appl. Phys. 2001; 40(1A/B): L71-L74.

[54] Ono T, Ooka Y, Miyajima H, Otani Y. Appl. Phys. Lett. 1999; 75(11):1622-1624.

[55] Gillingham DM, Linington I, Müller C, Bland JAC. J. Appl. Phys. 2003; 93(10): 7388-7389.

[56] Gillingham DM, Müller C, Bland JAC. J. Phys.: Cond. Matter. 2003; 15(19):L291-L296.

[57] Csonka Sz., Halbritter A, Mihály G, Jurdik E, Shklyarevskii OI, Speller S, van Kempen H. Phys. Rev. Lett. 2003; 90(11):116803.

[58] Untiedt C, Dekker DMT, Djukic D, van Ruitenbeek JM. Phys. Rev. B. 2004; 69:081401R.

[59] Arita M, Tajiri T, Hamada K, Miyagi H. J. Magn. Soc. Japn. 2005; 29(2):120-123, in Japanese.

[60] Ford EM, Dekker C, Schmid G. Appl. Phys. Lett. 1999; 75(3):421-423.

[61] Yakushiji K, Mitani S, Takanashi K, Takahashi S, Mekawa S, Imamura H, Fujimori H. Appl. Phys. Lett. 2001; 78(4):515-517.

[62] Hosoya H, Arita M, Hamada K, Takahashi Y, Higashi K, Oda K, Ueda M. J. Phys. D. 2006; 39(24):5103-5108.

[63] Arita M, Hirose R, Hamada K, Takahashi Y. Japn. J. Appl. Phys. 2006; 45(3B): 1946-1949.

[64] Arita M, Hirose R, Hamada K, Takahashi Y. Mater. Sci. Eng. C. 2006; 26(5-7):776-781.

[65] Simmons JG. J. Appl. Phys. 1963; 34(6):1793.

[66] Wulfhekel W, Klaua M, Ullmann D, Zavaliche F, Kirschner J, Urban R, Monchesky T, Heinrich B. Appl. Phys. Lett. 2001; 78(4):509-511.

[67] Kozicki MN, Park M, Mitkova M. IEEE Trans. Nanotechnol. 2005; 4(3):331-338.

[68] Sawa A. Mater. Today. 2008; 11(6):28-36.

[69] Chen A. Ionic Memory Technology. In: Kharton VV, editor. Solid State Electrochemistry II: Electrodes, Interfaces and Ceramic Membranes. 1st ed. Weinheim: Wiley-VCH; 2011.

[70] Kim KM, Hwang CS. Nanotechnol. 2011; 22(25):254002.

[71] Fujii T, Arita M, Hamada K, Takahashi Y, Sakaguch N. J. Appl. Phys. 2013; 113(8): 083701.

[72] Fujii T, Arita M, Takahashi Y, Fujiwara I. Appl. Phys. Lett. 2011; 98(21):212104.

[73] Fujii T, Arita M, Takahashi Y, Fujiwara I. J. Mater. Res. 2012; 27(6):886-896.

[74] Kudo M, Ohno Y, Hamada K, Arita M, Takahashi Y. ECS Trans. 2013; 58(5):19-25.

[75] Ohno Y, Hiroi T, Kudo M, Hamada K, Arita M, Takahashi Y. IEICE Tech. Rept ED. 2014; 113(449):89-94, in Japanese.

[76] Kudo M, Arita M, Ohno Y, Takahashi Y. Appl. Phys. Lett. 2014; 105(17):173504.

[77] Kondo H, Arita M, Fujii T, Kaji H, Moniwa M, Yamaguchi T, Fujiwara I, Yoshimaru M, Takahashi Y. Japn. J. Appl. Phys. 2011; 50(8):081101.

[78] Kwon DH, Kim KM, Jang JH, Jeon JM, Lee MH, Kim GH, Li XS, Park GS, Lee B, Han S, Kim M, Hwang CS. Nat. Nanotechnol. 2010; 5(2):148-153.

[79] Yang Y, Gao P, Gaba S, Chang T, Pan X, Lu W. Nat. Commun. 2012; 3:732.

[80] Liu Q, Sun J, Lv H, Long S, Yin K, Wan N, Li Y, Sun L, Liu M. Adv. Mater. 2012; 24(14): 1844-1849.

[81] Lee D, Seong D, Jo I, Xiang F, Dong R, Oh S, Hwang H. Appl. Phys. Lett. 2007; 90(12): 122104.

[82] Arita M, Kaji H, Fujii T, Takahashi Y. Thin Solid Films. 2012; 520(14):4762.

[83] Banno N, Sakamoto T, Iguchi N, Sunamura H, Terabe K, Hasegawa T, Aono M. IEEE Trans. Elect. Dev. 2008; 55(11):3283-3287.

[84] Bernard Y, Renard VT, Gonon P, Jousseaume V. Microelectr. Eng. 2011; 88(5):814-816.